Effect of caustics on the ray-based Born approximation

Libor Šachl

Charles University, Faculty of Mathematics and Physics, Department of Geophysics,
E-mail: sachl@karel.troja.mff.cuni.cz

Summary

3D P-wave synthetic seismograms in several 2D isotropic heterogeneous models have been computed using the first-order ray-based Born approximation and the ray theory. The Born approximation is computed in a 2D grid, and the background model is a 2D smooth heterogeneous isotropic velocity model. The seismograms have been computed for the total number of 37 receivers. The strange wavegroups are observed in the Born seismograms. The explanation is that these problems are caused by caustics on the direct wave. Three solutions are proposed. Seismograms corrected using one of these solutions are shown. Furthermore, particular wavegroups present in the Born seismograms and missing in the ray-theory seismograms are discussed.

Key words: Born approximation, ray theory, velocity model, caustic

1 Introduction

According to Červený (2001), the most common approaches to the investigation of seismic wavefields in complex structures are:

- methods based on direct numerical solutions of the elastodynamic equation, such as the finite-difference and finite-element methods, and
- approximate high-frequency asymptotic methods.

Let us focus on the ray theory, the representative of the second group. The ray theory has several important advantages compared, e.g., with finite differences: Large models and high frequencies do not represent any problem: the wavefield is divided into individual types of waves and so on. On the other hand, there are also disadvantages: the models must be smooth (must not change rapidly with respect to the Fresnel zone), the wavefield does not contain several types of waves (e.g., diffracted waves) and fails in the singular regions (shadow zones, caustics, etc.) (Brokešová, 2006).

It is desirable to benefit from the advantages of the ray theory and try to fix the disadvantages mentioned above. One possibility is to use a perturbation method. Perturbation methods are described by Červený et al. (2007): We assume that a model, in which we wish to study wave propagation, differs only little from another model called the background or reference model. The solution in the perturbed model can then be sought in the form of a power series in the deviations of the perturbed and background models. If only the first term of the series is considered, which is often the case, we speak

Seismic Waves in Complex 3-D Structures, Report 22, Charles University, Faculty of Mathematics and Physics, Department of Geophysics, Praha 2012, pp. 55-82

of the first-order perturbation expansion.

We use the first-order ray-based Born approximation. We use the ray theory to compute and discretize the appropriate quantities in the computational grid in the background model. The Born approximation uses these quantities to compute the seismograms. A large advantage of the ray-based Born approximation is computational efficiency (Jin et al., 1992). The method is applicable to the larger class of models rather than the ray theory because it requires the background model, not the original (perturbed) model to be smooth. Furthermore, the method models diffracted waves, which can carry valuable information for seismic imaging, see Moser (2012) or Šachl (2011). It is not possible to compute reflected waves without the diffracted waves by the Born approximation. On the other hand, it is possible to model the P-P (the incident P wave, the scattered P wave), P-S, S-P and S-S scattering separately.

In this paper we show that the first-order ray-based Born approximation can also have problems in some situations, which are connected with caustics. We also provide a solution of how to get rid of these problems. The motivation to study the effects of caustics on the ray-based Born approximation could be the papers by Moser (1997) and Thierry (1999). Moser (1997) studied the performance of the ray-Born inversion. He concluded that the presence of caustics connected to multipathing degrades the image. It was suggested to use the first arrival or the most energetic arrival inversion, but the author's experience is that the image is improved only to a slight degree. Thierry (1999) tested the 2D ray-Born migration/inversion algorithm. He experienced similar difficulties and claimed that in the presence of caustics the full recovery of the amplitude of velocity perturbation is not possible.

The paper is organized as follows: the theory of the ray-based Born approximation is given in Section 2. The models where we compute the seismograms are presented in Section 3. The computational setup is discussed in Section 4. The effects of caustic on the direct and reflected wave are discussed in Section 5 and Section 6; these two sections are the key parts of the paper.

2 The ray-based Born approximation in an isotropic medium, with point-source and high-frequency approximation

Consider an isotropic medium. We insert the expression

$$c_{ijkl} = \lambda\delta_{ij}\delta_{kl} + \mu(\delta_{ik}\delta_{jl} + \delta_{il}\delta_{jk}) \tag{1}$$

for the components of the elastic tensor in the isotropic solid into the first-order Born approximation (Červený, 2001, eq. 2.6.18)

$$\begin{aligned}\Delta u_n(\mathbf{x},\omega) = \int_\Omega \big[&\omega^2 u_i(\mathbf{x}',\omega)\Delta\rho(\mathbf{x}')G_{ni}(\mathbf{x},\mathbf{x}',\omega) \\ &- u_{k,l}(\mathbf{x}',\omega)\Delta c_{ijkl}(\mathbf{x}')G_{ni,j}(\mathbf{x},\mathbf{x}',\omega)\big]\,d^3\mathbf{x}',\end{aligned} \tag{2}$$

where ω is the circular frequency, $\Delta c_{ijkl}(\mathbf{x}')$ and $\Delta\rho(\mathbf{x}')$ are the perturbations of elastic moduli and density, Ω is the domain where these perturbations are non-zero, $u_i(\mathbf{x}',\omega)$ is the solution of the elastodynamic equation for the background medium, $G_{ij}(\mathbf{x},\mathbf{x}',\omega)$ is

the Green function in the background medium and $G_{ij,k}(\mathbf{x},\mathbf{x}',\omega)$ is the spatial derivative of the Green function with respect to x'_k. The Einstein summation convention is used. Moser (2012) points out that no special requirements regarding the smoothness of $\Delta\rho(\mathbf{x}')$ and $\Delta c_{ijkl}(\mathbf{x}')$ are necessary. We further use the reciprocity of the Green function $G_{ij}(\mathbf{x},\mathbf{x}',\omega) = G_{ji}(\mathbf{x}',\mathbf{x},\omega)$ to obtain

$$\begin{aligned}\Delta u_i(\mathbf{x},\omega) = \int_\Omega \big[&\omega^2 \Delta\rho(\mathbf{x}') G_{ji}(\mathbf{x}',\mathbf{x},\omega) u_j(\mathbf{x}',\omega) \\ &- \Delta\lambda(\mathbf{x}') G_{ji,j}(\mathbf{x}',\mathbf{x},\omega) u_{k,k}(\mathbf{x}',\omega) \\ &- \Delta\mu(\mathbf{x}') G_{ki,j}(\mathbf{x}',\mathbf{x},\omega)(u_{k,j}(\mathbf{x}',\omega) + u_{j,k}(\mathbf{x}',\omega))\big] d^3\mathbf{x}', \end{aligned} \tag{3}$$

where $G_{ij,k}(\mathbf{x}',\mathbf{x},\omega)$ is the spatial derivative of the Green function with respect to x'_k. Note that the reciprocity is applied for numerical reasons only. We assume that a point source is located at point $\mathbf{x}^s$. The wavefield and the Green function in the background model are computed using the ray theory. Let us decompose the wavefield and the Green function into amplitudes a_i, A_{ij} and phase terms $\exp(i\omega\tau(\mathbf{x}'))$, $\exp(i\omega T(\mathbf{x}'))$. We arrive at the ray-theory approximation

$$u_i(\mathbf{x}',\omega) = a_i(\mathbf{x}') \exp(i\omega\tau(\mathbf{x}')), \tag{4}$$

$$G_{ij}(\mathbf{x}',\mathbf{x},\omega) = A_{ij}(\mathbf{x}',\mathbf{x}) \exp(i\omega T(\mathbf{x}')), \tag{5}$$

where $\tau(\mathbf{x}')$ is the travel time from $\mathbf{x}^s$ to $\mathbf{x}'$, i.e. from the point source to an integration point, and $T(\mathbf{x}')$ is the travel time from $\mathbf{x}$ to $\mathbf{x}'$, i.e. from the receiver to an integration point. We compute the travel time solving the eikonal equation; the amplitude is determined using dynamic ray tracing, see Červený (2001).

We now apply the high-frequency approximation of the spatial derivatives,

$$u_{i,j}(\mathbf{x}',\omega) \approx i\omega a_i(\mathbf{x}') p_j(\mathbf{x}') \exp(i\omega\tau(\mathbf{x}')), \tag{6}$$

$$G_{ij,k}(\mathbf{x}',\mathbf{x},\omega) \approx i\omega A_{ij}(\mathbf{x}',\mathbf{x}) P_k(\mathbf{x}') \exp(i\omega T(\mathbf{x}')), \tag{7}$$

where $p_i(\mathbf{x}')$ is the spatial derivative of travel time $\tau(\mathbf{x}')$ with respect to x'_i and $P_i(\mathbf{x}')$ is the spatial derivative of travel time $T(\mathbf{x}')$ with respect to x'_i. $G_{ij,k}(\mathbf{x}',\mathbf{x},\omega)$ is the spatial derivative of the Green function with respect to x'_k.

Using equations (4), (5), (6) and (7), equation (3) becomes

$$\begin{aligned}\Delta u_i(\mathbf{x},\omega) = \omega^2 \int_\Omega &\exp[i\omega(\tau(\mathbf{x}') + T(\mathbf{x}'))] \\ &[\Delta\rho(\mathbf{x}') A_{ji}(\mathbf{x}',\mathbf{x}) a_j(\mathbf{x}') \\ &+ \Delta\lambda(\mathbf{x}') A_{ji}(\mathbf{x}',\mathbf{x}) P_j(\mathbf{x}') a_k(\mathbf{x}') p_k(\mathbf{x}') \\ &+ \Delta\mu(\mathbf{x}') A_{ki}(\mathbf{x}',\mathbf{x}) P_j(\mathbf{x}')(a_k(\mathbf{x}') p_j(\mathbf{x}') + a_j(\mathbf{x}') p_k(\mathbf{x}'))] d^3\mathbf{x}'. \end{aligned} \tag{8}$$

If the source and receiver are situated in symmetry plane S of a 2D model, we can compute the Born approximation numerically in a 2D slice and perform the remaining one-dimensional integration analytically in the direction perpendicular to the slice, applying the method of stationary phase. Let us introduce a Cartesian coordinate system in which x_1 is the horizontal coordinate, x_3 is the vertical coordinate and $x_2 = 0$ for all points in

the slice. The equation in the acoustic medium is derived in Červený and Coppoli (1992). The case of the elastic medium is treated in Foss et al. (2005) and Bansal and Sen (2010); the resulting equation has the form

$$\Delta u_i(\mathbf{x},\omega) = \omega^2 \int_S \sqrt{\frac{\pi}{\omega(\tau_{,22}(\mathbf{x}') + T_{,22}(\mathbf{x}'))}}(1+i)\exp[i\omega(\tau(\mathbf{x}') + T(\mathbf{x}'))] \\ [\Delta\rho(\mathbf{x}')A_{ji}(\mathbf{x}',\mathbf{x})a_j(\mathbf{x}') \\ + \Delta\lambda(\mathbf{x}')A_{ji}(\mathbf{x}',\mathbf{x})P_j(\mathbf{x}')a_k(\mathbf{x}')p_k(\mathbf{x}') \\ + \Delta\mu(\mathbf{x}')A_{ki}(\mathbf{x}',\mathbf{x})P_j(\mathbf{x}')(a_k(\mathbf{x}')p_j(\mathbf{x}') + a_j(\mathbf{x}')p_k(\mathbf{x}'))]d^3\mathbf{x}', \quad (9)$$

where $\tau_{,22}(\mathbf{x}')$ and $T_{,22}(\mathbf{x}')$ are the second spatial derivatives of travel time $\tau(\mathbf{x}')$ and travel time $T(\mathbf{x}')$ in the direction of the x_2 axis at point $\mathbf{x}'$, respectively. Thus, we can compute the Born approximation in the same way as in a 3D model, the only modification being the multiplication of the integrand in the Born integral by term

$$I_{cor} = \sqrt{\frac{\pi}{\omega(\tau_{,22}(\mathbf{x}') + T_{,22}(\mathbf{x}'))}}(1+i). \quad (10)$$

The validity of the ray-based Born approximation relies upon the validity of the Born approximation and the ray theory. The Born approximation requires the first-order scattered wave to be much smaller than the background wave. This condition can be satisfied using a low frequency or a small scatterer. On the other hand, if we construct a realistic background in order to obtain a small scatterer, the ray theory may be invalid (Moser, 1997). The ray theory requires the wavelength to be much smaller than the characteristic length of the background model. Additionally, the ray theory is not valid in caustics or in their vicinity (Červený, 2001).

3 Perturbed models and the background model

The models where we would like to obtain seismograms (perturbed models) are referred to as P1-j-10%, j $\in \{1,2,3,4,5,6,7,8,9,10,15\}$. The models are constructed from model P1I and smooth model P1. The background model is a smooth model P1. Model P1I and smooth model P1 were both created by Bulant and Martakis (2011). All models in this paper are 2D isotropic heterogeneous velocity models situated in rectangle (0 km, 47.3 km) $\times$ (0 km, 6 km).

P-wave velocity v_p in smooth model P1 is depicted in Figure 1. S-wave velocity $v_s = v_p/\sqrt{3}$. Density $\rho = 1000$ kg/m^3 everywhere. Figure 1 of the P-wave velocities is created using a grid which contains 4730×600 grid points. The lowest and largest values of the discretized P-wave velocities are $(v_p)_{min} \approx 4.64$ km/s and $(v_p)_{max} \approx 5.93$ km/s respectively.

Model P1I is quite complicated because it is composed of 16 blocks separated by smooth interfaces. The largest absolute value of the difference between P-wave velocity in model P1I and P-wave velocity in smooth model P1 is $|\Delta v_p|_{max} \approx 0.21$ km/s.

The density in the perturbed models is the same as in the background model and equal to $\rho = 1000$ kg/m^3 everywhere. S-wave velocity $v_s = \frac{v_p}{\sqrt{3}}$. The P-wave velocity in each model is the same as in the background model except for one domain. The P-wave velocity

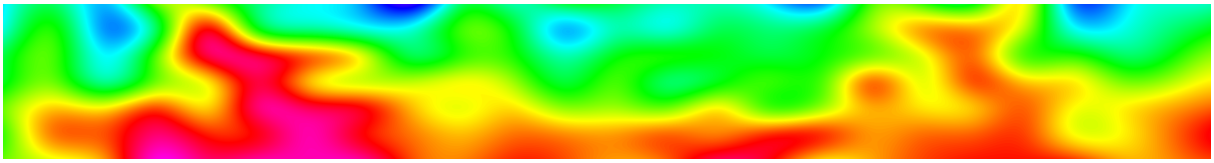

Figure 1: P-wave velocity in smooth model P1. The P-wave velocity ranges from 4.64 km/s to 5.93 km/s. The colour changes from blue to green and red as the P-wave velocity grows.

in each of these domains is equal to the P-wave velocity in the background model plus 10% of the perturbation between the background model and model P1I. The perturbation is reduced to 10% in order to satisfy the sufficiently small differences between the perturbed and the background model. This is the requirement of the Born approximation. The P-wave velocity perturbation between model P1-j-10% and the background model is depicted for each model P1-j-10%, $j \in \{1, 2, 3, 4, 5, 6, 7, 8, 9, 10, 15\}$, in Figures 2 to 12.

Figure 2: P-wave velocity perturbation between model P1-1-10% and the background model. Positive perturbations are red, negative perturbations are green. Zero perturbations are yellow.

Figure 3: P-wave velocity perturbation between model P1-2-10% and the background model. Positive perturbations are red, negative perturbations are green. Zero perturbations are yellow.

Figure 4: P-wave velocity perturbation between model P1-3-10% and the background model. Positive perturbations are red, negative perturbations are green. Zero perturbations are yellow.

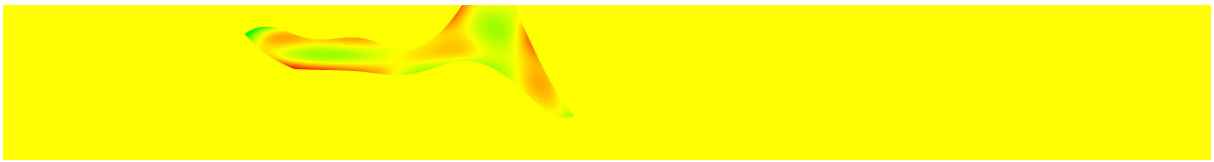

Figure 5: P-wave velocity perturbation between model P1-4-10% and the background model. Positive perturbations are red, negative perturbations are green. Zero perturbations are yellow.

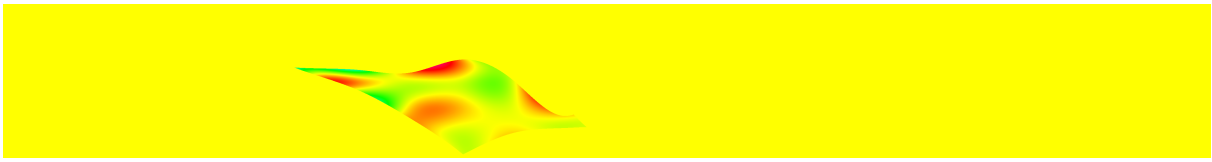

Figure 6: P-wave velocity perturbation between model P1-5-10% and the background model. Positive perturbations are red, negative perturbations are green. Zero perturbations are yellow.

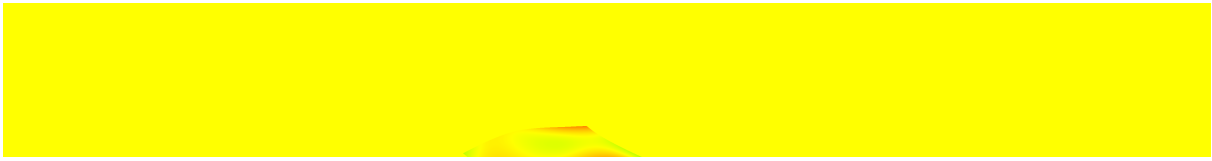

Figure 7: P-wave velocity perturbation between model P1-6-10% and the background model. Positive perturbations are red, negative perturbations are green. Zero perturbations are yellow.

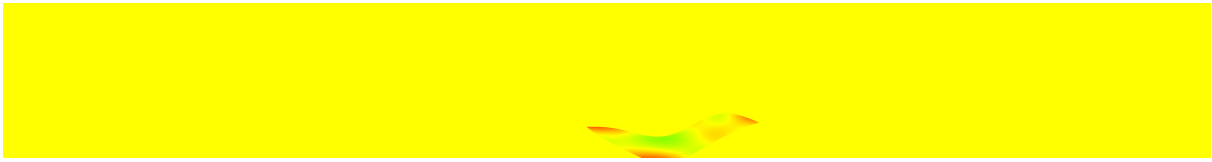

Figure 8: P-wave velocity perturbation between model P1-7-10% and the background model. Positive perturbations are red, negative perturbations are green. Zero perturbations are yellow.

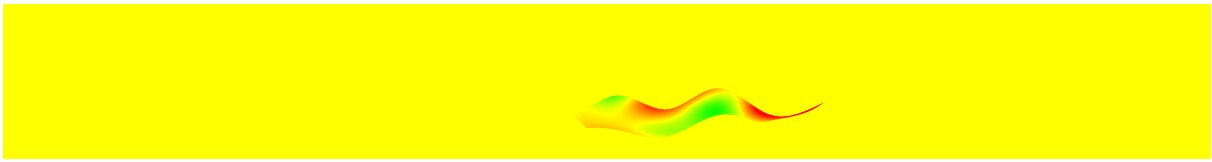

Figure 9: P-wave velocity perturbation between model P1-8-10% and the background model. Positive perturbations are red, negative perturbations are green. Zero perturbations are yellow.

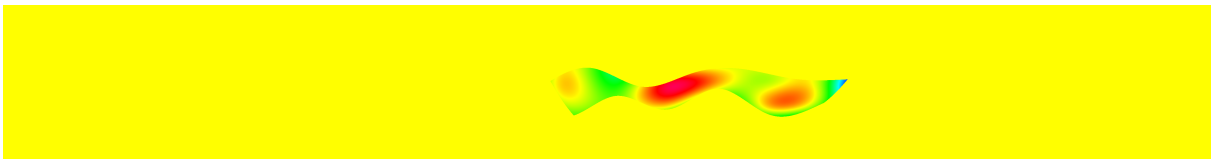

Figure 10: P-wave velocity perturbation between model P1-9-10% and the background model. Positive perturbations are red, negative perturbations are green and blue. Zero perturbations are yellow.

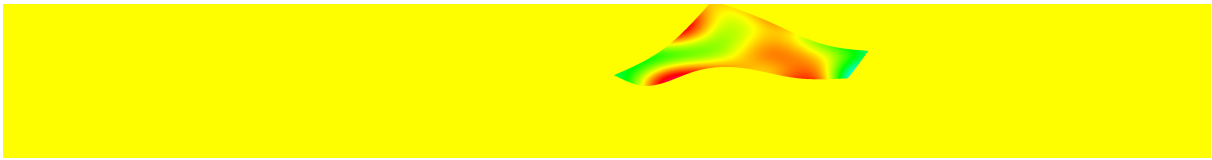

Figure 11: P-wave velocity perturbation between model P1-10-10% and the background model. Positive perturbations are red, negative perturbations are green and blue. Zero perturbations are yellow.

Figure 12: P-wave velocity perturbation between model P1-15-10% and the background model. Positive perturbations are red, negative perturbations are green. Zero perturbations are yellow.

4 Computation of the seismograms

We use the following Cartesian coordinate system: x_1 is the horizontal coordinate, increasing from the left to the right; x_3 is the vertical coordinate, increasing downwards. The origin of the coordinate system is in the upper left corner of the model.

Motivated by Bulant and Martakis (2011), we chose 37 receivers placed at the upper model boundary. The first receiver has the horizontal coordinate $x_1 = 16$ km. The spacing between the receivers is 0.5 km, therefore, the last receiver has the horizontal coordinate $x_1 = 34$ km.

The explosive source is also placed at the upper model boundary, $x_1 = 25$ km, $x_3 = 0$ km. Its position is the same as the position of the 19th receiver. The source time function is a Gabor signal with a prevailing frequency of 10 Hz, filtered by a frequency filter which is non-zero only for frequencies f, 1 Hz $< f <$ 20 Hz. There is a cosine tapering for 1 Hz $< f <$ 2 Hz and 19 Hz $< f <$ 20 Hz while for 2 Hz $< f <$ 19 Hz the filter is equal to one. Only P waves are considered.

The rays are shot into the whole lower half-plane. We use the basic system of rays containing 121 rays, which covers the straight angle into which the rays are shot.

The Born seismograms are computed using these settings and compared with the ray-theory seismograms. The detailed analysis of the seismograms is not presented in this paper, but can be found in Šachl (2012). Here we focus just on the effects caused by the caustics.

5 Caustics on the direct wave

We start with the seismograms computed in models P1-5-10% and P1-6-10%. The seismograms are depicted in Figure 20 and Figure 22, respectively. Some strange wavegroups can be observed in the computed seismograms. They are marked in ghost green in Figures 20 and 22. Let us have several close receivers. If the strange wavegroups are present in the seismograms computed for these receivers, they usually differ significantly among themselves, see Figure 20. The amplitude is different, the phase can change, sometimes the signals are not at all similar. On the other hand, the wavegroups present in several close receivers have similar travel times. Our explanation is that these wavegroups are caused by the caustics on the direct wave.

The study of the strange wavegroups in seismograms computed in model P1-6-10% seems to be promising, because there are just two strange wavegroups with similar travel times in the seismograms. These strange wavegroups appear for the receivers with horizontal coordinates $x_1 = 33.0$ k m and $x_1 = 33.5$ km. The Born approximation is computed using the grid, in which the required quantities are discretized. The computation of the quantities at the gridpoints of the computational grid is the following: the model volume is decomposed into ray cells on the direct wave using controlled initial-value ray tracing, and the interpolation within these ray cells follows. The algorithm is described by Bulant (1999). Thus, it is desirable to check the rays and the ray coverage of Block 6. The Born approximation uses both the Green function from the source and from the receiver. The Green function from the source is the same for all receivers, therefore, if there are any problems, they should be caused by the Green function from the receiver. The Figures 13, 14, 15, 16 depict the ray coverage of Block 6 in shooting rays from the receivers at $x_1 = 32.5$ km, $x_1 = 33.0$ km, $x_1 = 33.5$ km, $x_1 = 34.0$ km.

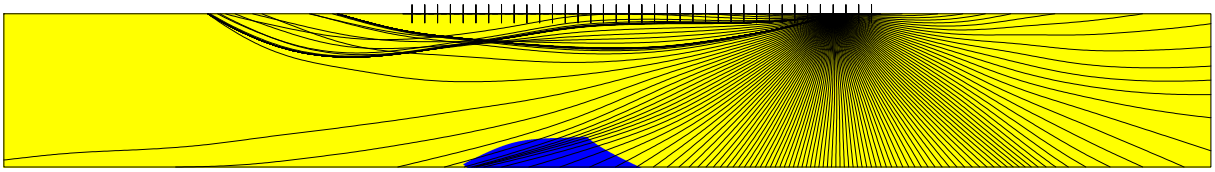

Figure 13: Coverage of the background model with the rays in shooting from the position of the receiver at $x_1 = 32.5$ km (the 4th receiver from the right). The receivers are placed at the upper model boundary and their positions are marked by abscissae. The points containing non-zero P-wave velocity perturbations between model P1-6-10% and smooth background model P1 are plotted in blue.

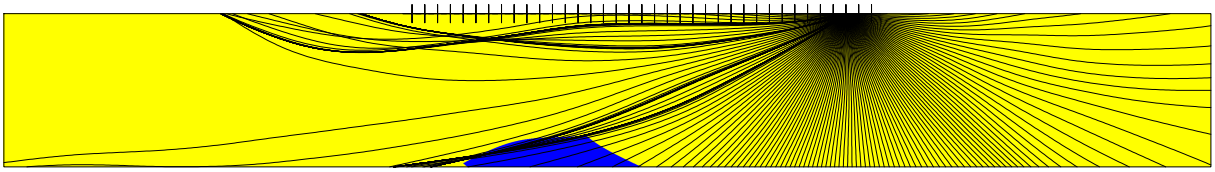

Figure 14: Coverage of the background model with the rays in shooting from the position of the receiver at $x_1 = 33.0$ km (the 3rd receiver from the right).

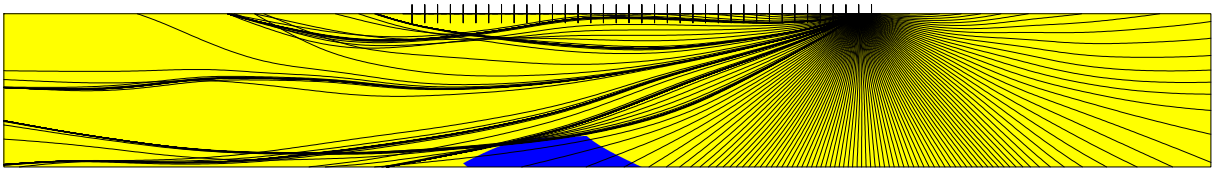

Figure 15: Coverage of the background model with the rays in shooting from the position of the receiver at $x_1 = 33.5$ km (the 2nd receiver from the right).

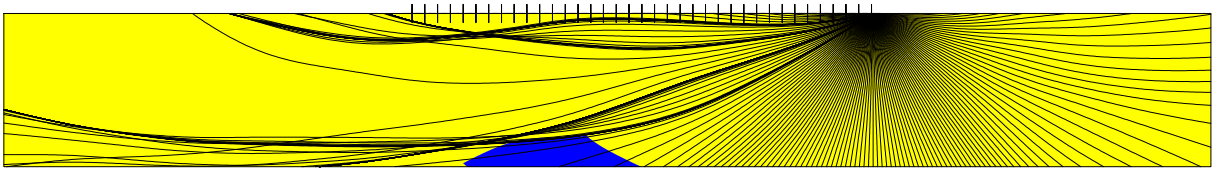

Figure 16: Coverage of the background model with the rays in shooting from the position of the receiver at $x_1 = 34.0$ km (the 1st receiver from the right).

The intersection of rays can be seen in Figure 14 and Figure 15. These figures correspond to the receivers with the strange wavegroups in the seismograms. The places where two neighbouring rays intersect are called caustics. Caustics often cause difficulties in modelling wavefields. They produce infinite ray amplitudes, phase shifts of signals and triplications of the wavefront. Caustics usually appear in wavefields propagating in heterogeneous media or media with curved interfaces (Vavryčuk, 2003).

We mostly worry about the infinite ray amplitudes. This problem is typical for the ray theory and is caused by the vanishing ray Jacobian (and its square root called the geometrical spreading), see Červený (2001, sec. 3.10.5). We perform the following experiment:

First, we find the "largest values" of the discretized amplitudes of the Green function. We analyze component G_{11} of Green function G_{ij}. The Green function is discretized in the grid with grid intervals of 0.005 km. The "largest values" of the amplitudes are one order larger than the typical values of the amplitude. The gridpoints with the "largest values" are marked in Figures 17 and 18 by red crosses. Note that only the gridpoints which lie in Block 6 are shown.

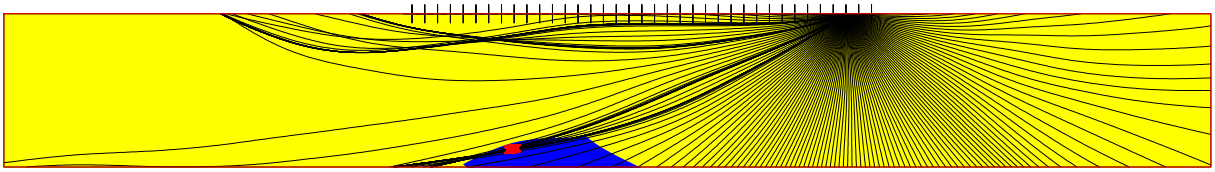

Figure 17: Positions of the "largest values" of the amplitudes of component G_{11} of the Green function marked by red crosses. The rays are shot in the background model from the position of the receiver at $x_1 = 33.0$ km (the 3rd receiver from the right). The receivers are placed at the upper model boundary and their positions are marked by abscissae. The points containing non-zero P-wave velocity perturbations between model P1-6-10% and smooth background model P1 are plotted in blue.

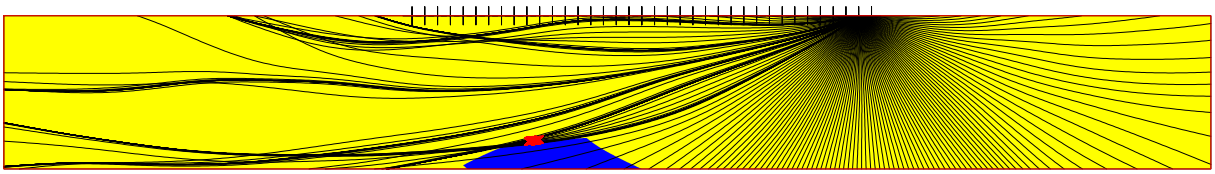

Figure 18: Positions of the "largest values" of the amplitudes of component G_{11} of the Green function marked by red crosses. The rays are shot in the background model from the position of the receiver at $x_1 = 33.5$ km (the 2nd receiver from the right).

The red crosses in Figures 17 and 18 correspond to the position of the caustic. Do not be mislead by the positions of the intersections of thicker lines created by several near rays. They have a slightly different meaning. The caustic is located closer to the source.

Second, we compute the Born seismograms for the receivers at $x_1 = 33.0$ km and $x_1 = 33.5$ km using 2 small grids. The first small grid is the grid for the receiver at $x_1 = 33.0$ km; it contains the gridpoints marked by the red crosses in Figure 17. The second small grid is the grid for the receiver at $x_1 = 33.5$ km; it contains the gridpoints marked by the red crosses in Figure 18. The original grid is a regular rectangular grid which covers Block 6 (not the whole model). The second small grid is composed of only approximately 2 % of the original gridpoints. The first small grid is even smaller; it contains about 0.3 % of the original gridpoints. The newly computed Born seismograms are compared with the original seismograms in Figure 19. The seismograms are ten times enlarged to see the details better.

Figure 19 shows that the Born seismograms computed using the small grids do not contain the waves diffracted from the edges of Block 6. This is not surprising, as neither of the two small grids covers these edges. However, the strange wavegroups do not differ too much. There are some differences, but they can be caused by the diffractions at the boundaries of the small grid.

5.1 Proposed solutions of the problem

We have at least 3 possibilities how to solve the observed problem:
1. Use a smoother background model, where caustics are not present.
2. Dampen the "largest amplitudes" choosing an appropriate cut-off.
3. Use Gaussian wave packets, which do not suffer from infinite amplitudes in the caustics.

The first possibility could work in some models. However, excessively violent smoothing is not desirable, because the Born approximation requires the background model to be close to the perturbed model.

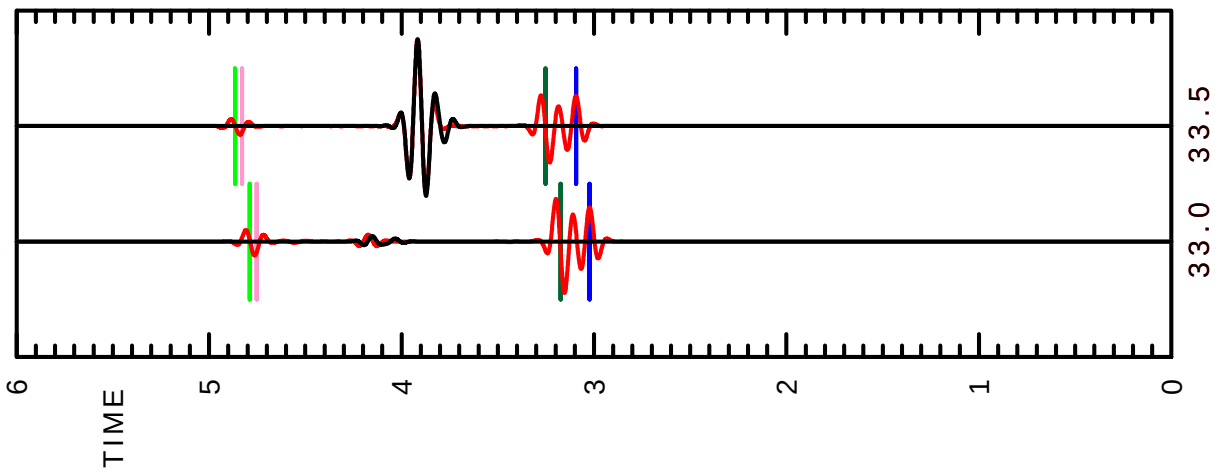

Figure 19: The Born seismograms computed in model P1-6-10% using the grid which covers the whole of Block 6 (black) and using the small grids which contain the gridpoints with the "largest values" of the amplitude of component G_{11} of the Green function (red). The seismograms are computed for the receivers at $x_1 = 33.5$ km and at $x_1 = 34.0$ km.

The second possibility is easy to accomplish, but the value of the cut-off depends on the user.

The third possibility sounds interesting and it is probably the only correct solution. Unfortunately, it requires new approach to the computation of the Born approximation, new programs, etc..

5.2 Corrected seismograms

We tested the second possibility. The seismograms computed in models P1-5-10% and P1-6-10% using appropriate cut-offs are depicted in Figures 21 and 23, respectively. The strange wavegroups in the seismograms computed in model P1-5-10% are still visible, but their amplitudes are much smaller now. Even better results are obtained for the corrected seismograms computed in model P1-6-10%. The strange wavegroups virtually disappeared from the seismograms computed in model P1-6-10%.

The discussed problem is observed also in the seismograms computed in models P1-1-10%, P1-2-10%, P1-3-10%, P1-4-10%, P1-10-10%, P1-15-10%. The coresponding seismograms computed using no amplitude cut-off and using the amplitude cut-offs are depicted in Figures 24 and 25, Figures 26 and 27, Figures 28 and 29, Figures 30 and 31, Figures 32 and 33, Figures 34 and 35, respectively.

The problem of this method is that the choice of the value of the cut-off is not unique. We choose the value in order to preserve the genuine waves and dampen the strange waves. The genuine waves are the waves reflected from the interfaces of the block and the diffracted waves, see also Šachl (2012).

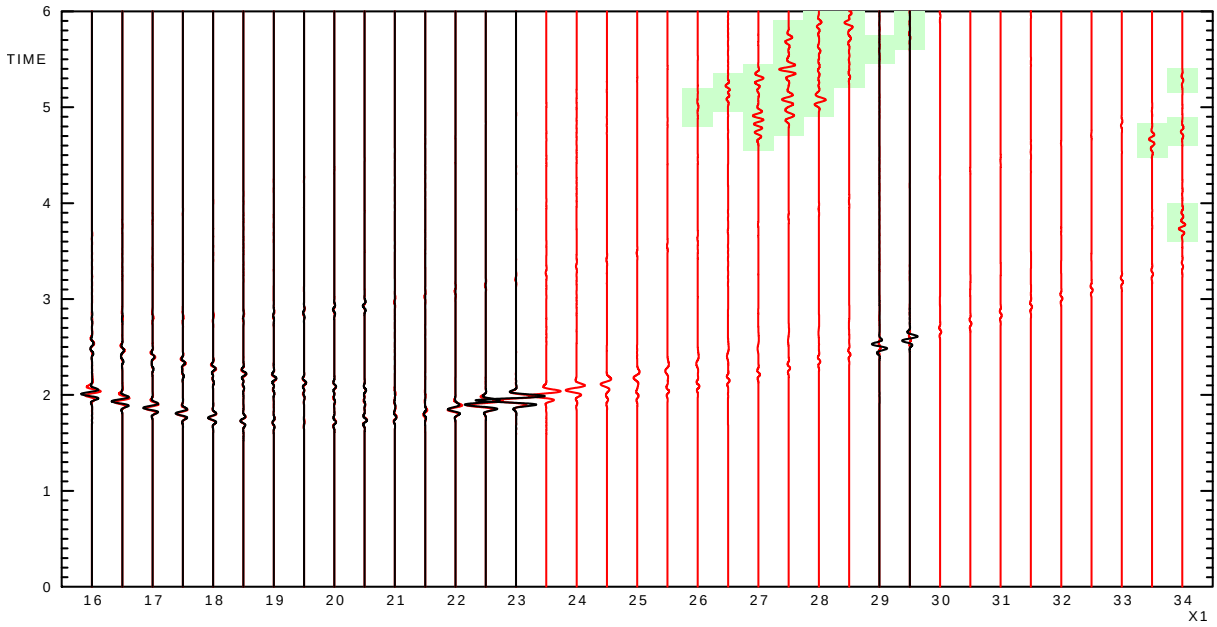

Figure 20: Born (red) and ray-theory (black) seismograms computed in model P1-5-10% using no amplitude cut-off. The strange wavegroups in the Born seismograms marked in ghost green are caused by the caustics on the direct wave.

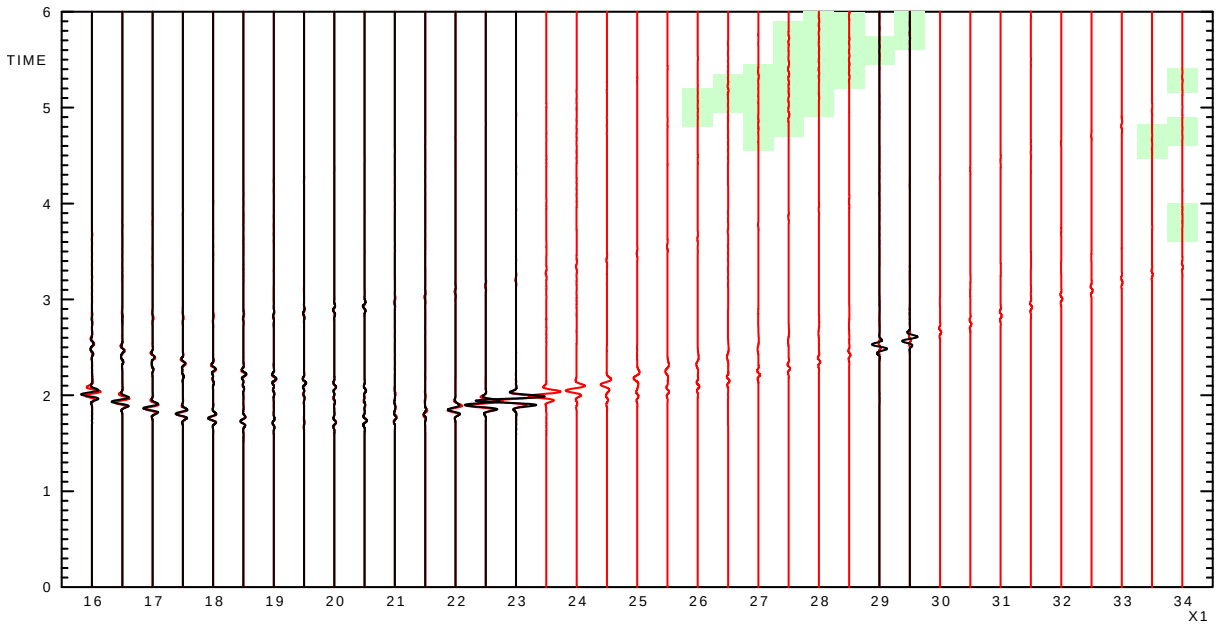

Figure 21: Born (red) and ray-theory (black) seismograms computed in model P1-5-10% using the amplitude cut-offs. The strange wavegroups in the Born seismograms marked in ghost green are damped.

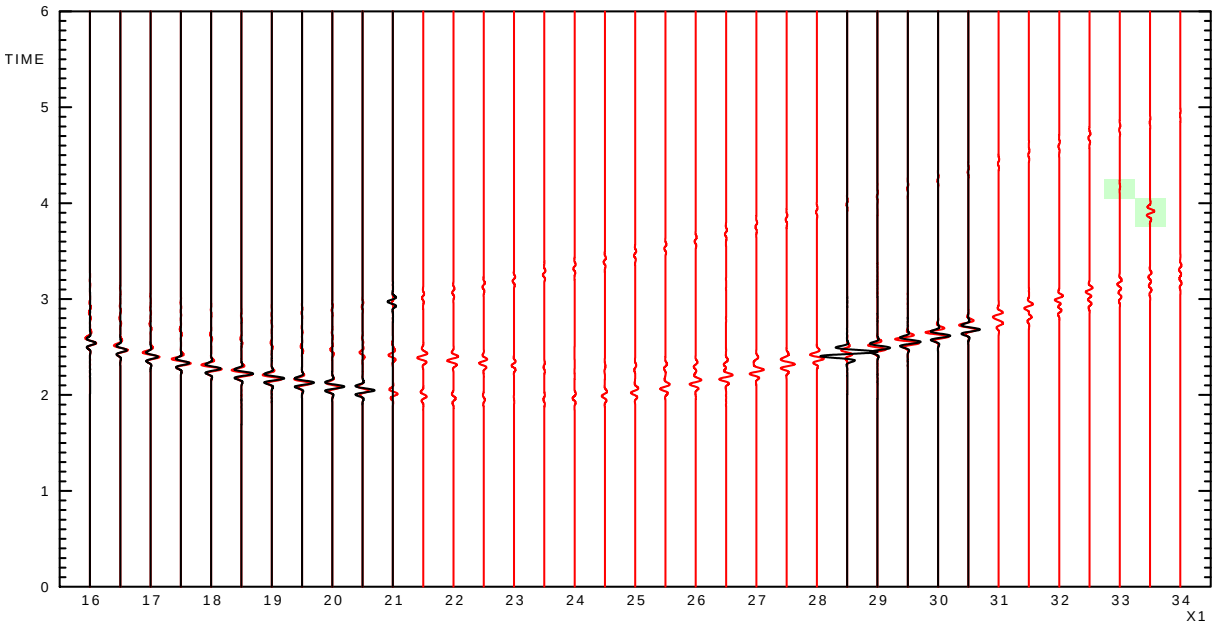

Figure 22: Born (red) and ray-theory (black) seismograms computed in model P1-6-10% using no amplitude cut-off. The strange wavegroups in the Born seismograms marked in ghost green are caused by the caustics on the direct wave.

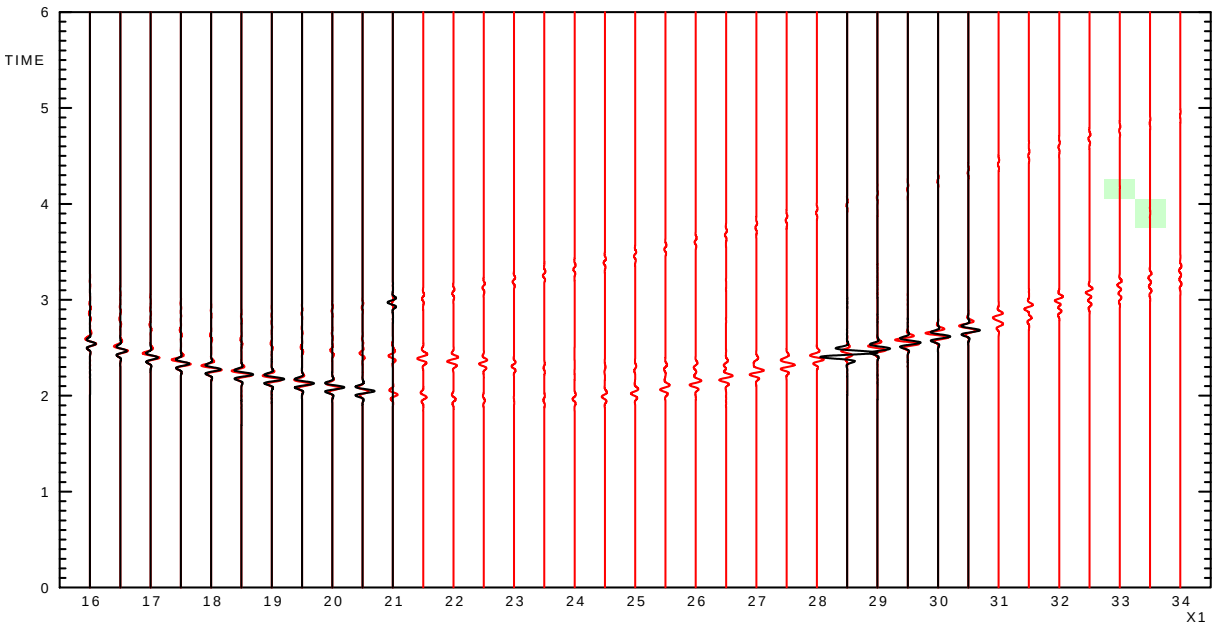

Figure 23: Born (red) and ray-theory (black) seismograms computed in model P1-6-10% using the amplitude cut-offs. The strange wavegroups in the Born seismograms marked in ghost green virtually disappeared.

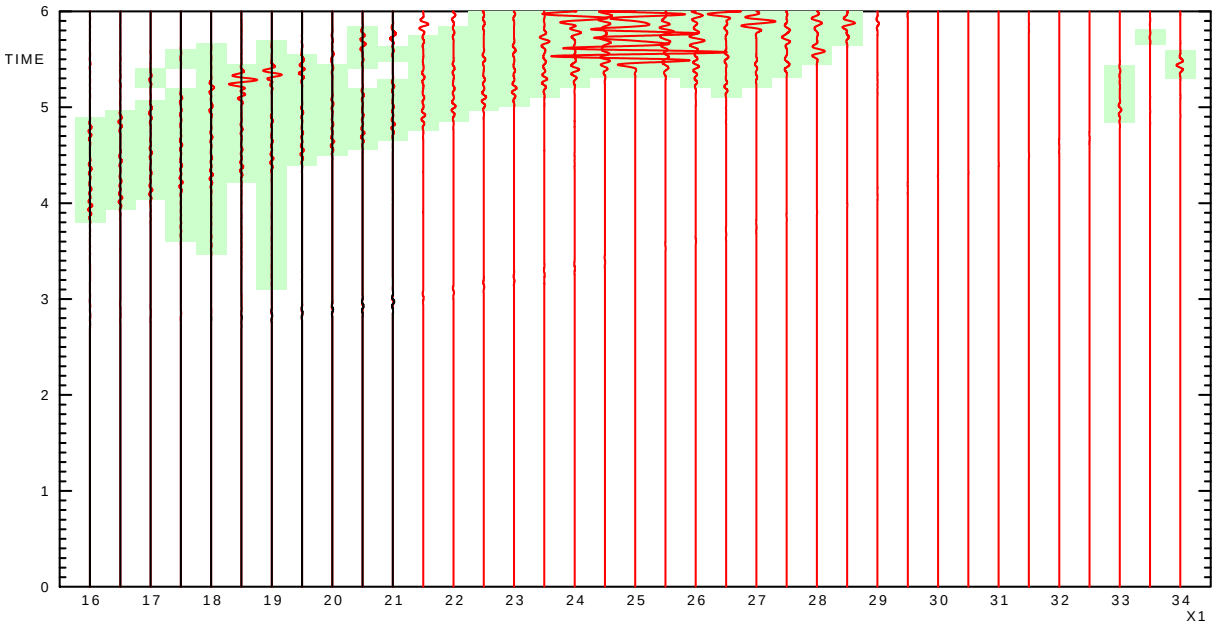

Figure 24: Born (red) and ray-theory (black) seismograms computed in model P1-1-10% using no amplitude cut-off.

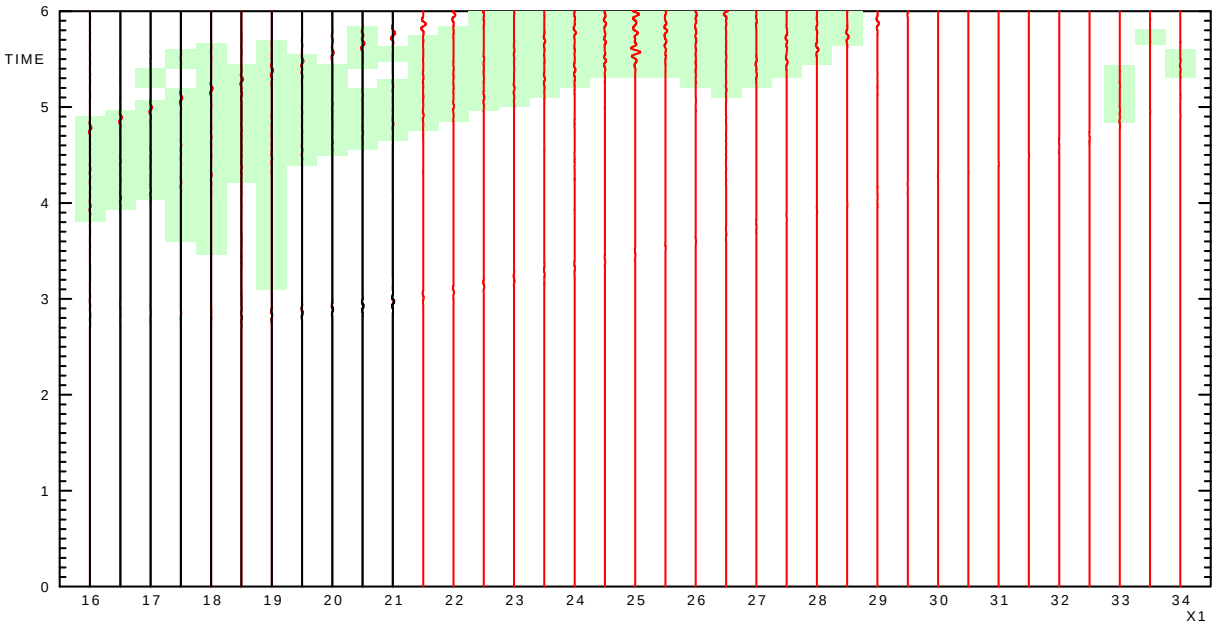

Figure 25: Born (red) and ray-theory (black) seismograms computed in model P1-1-10% using the amplitude cut-offs.

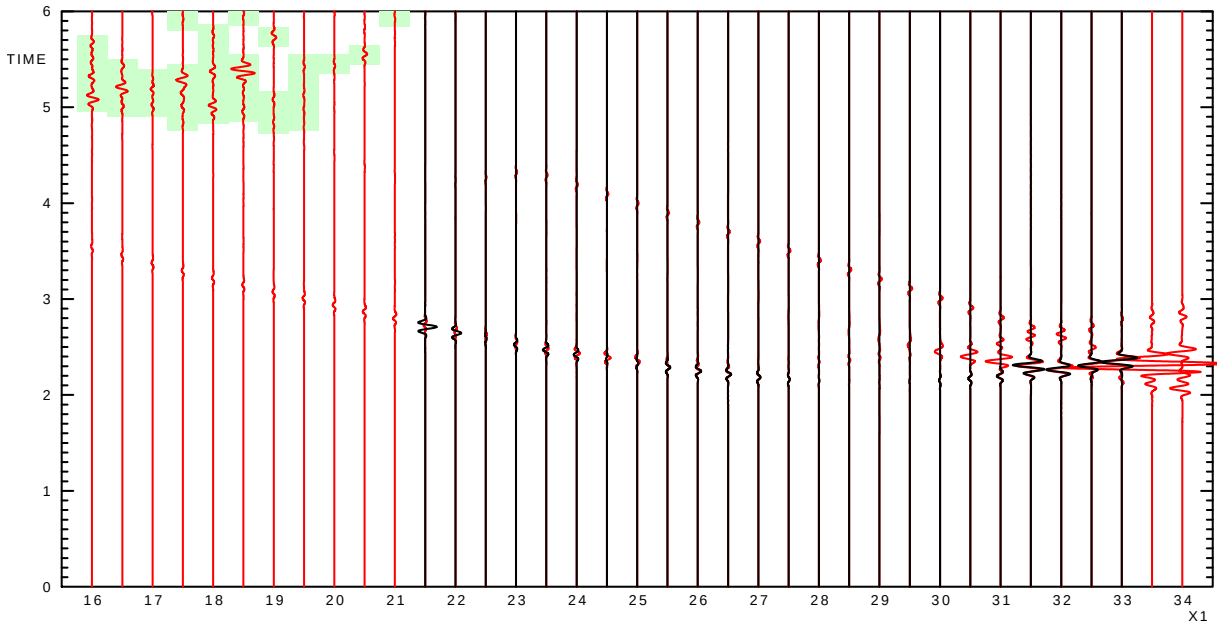

Figure 26: Born (red) and ray-theory (black) seismograms computed in model P1-2-10% using no amplitude cut-off.

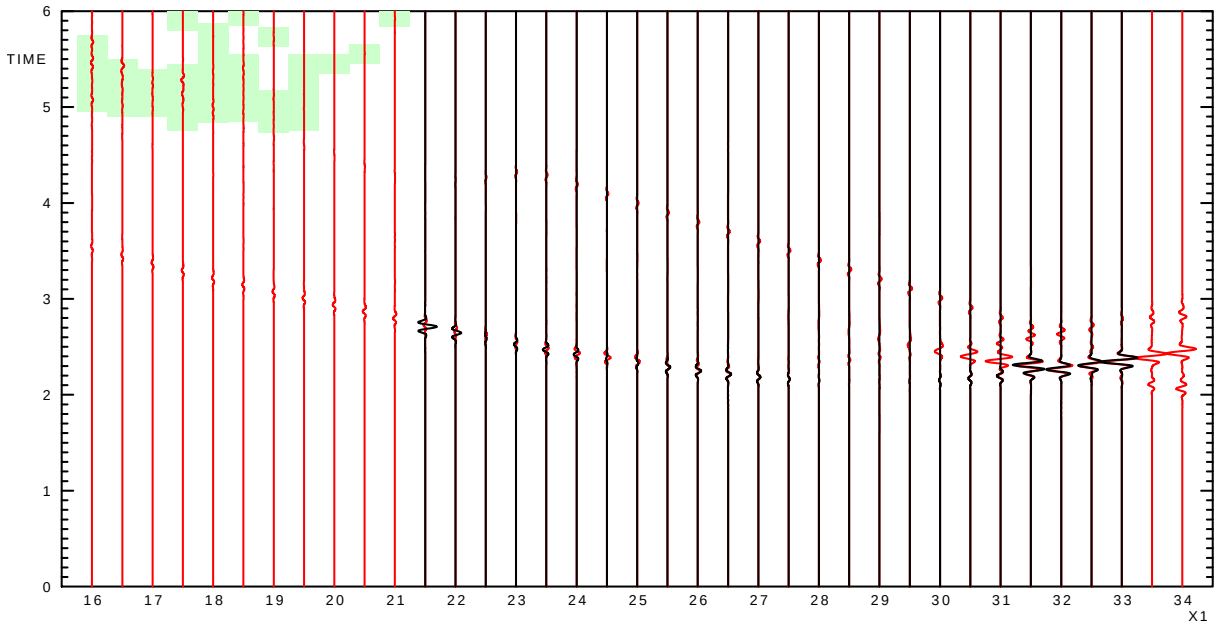

Figure 27: Born (red) and ray-theory (black) seismograms computed in model P1-2-10% using the amplitude cut-offs.

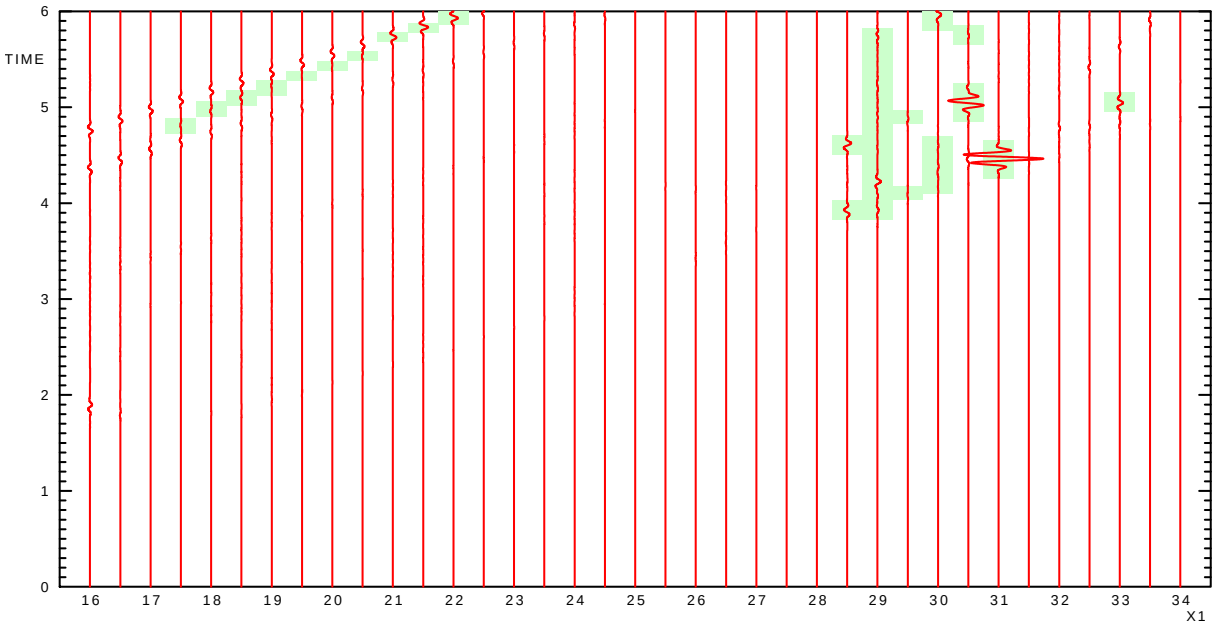

Figure 28: Born (red) and ray-theory (black) seismograms computed in model P1-3-10% using no amplitude cut-off.

Figure 29: Born (red) and ray-theory (black) seismograms computed in model P1-3-10% using the amplitude cut-offs.

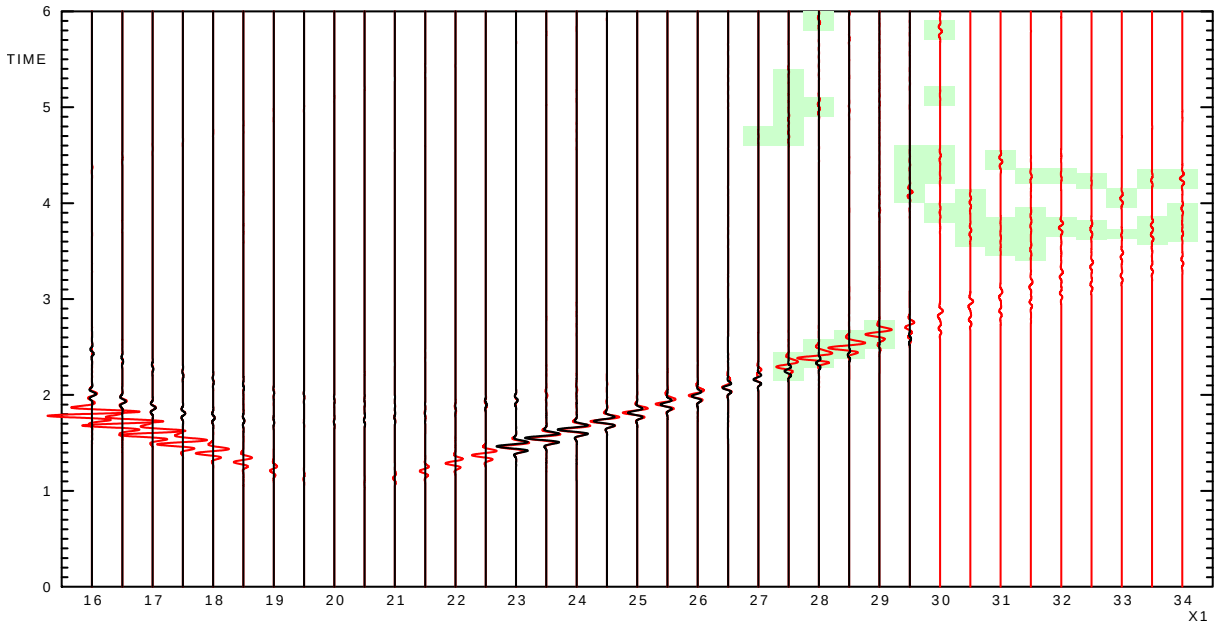

Figure 30: Born (red) and ray-theory (black) seismograms computed in model P1-4-10% using no amplitude cut-off.

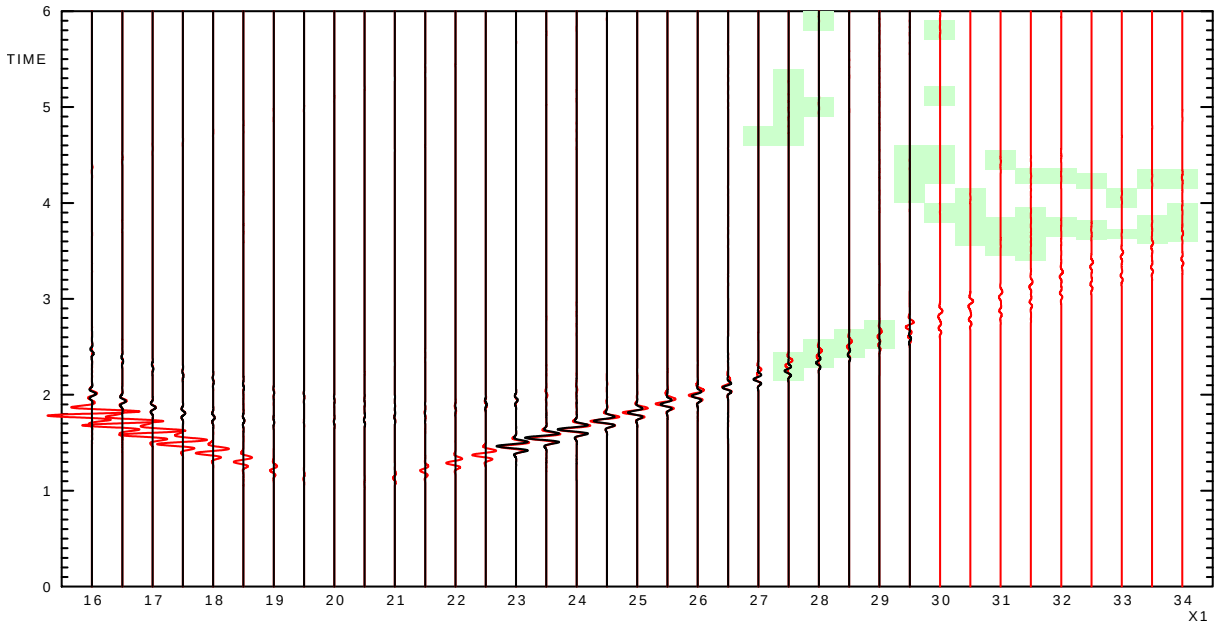

Figure 31: Born (red) and ray-theory (black) seismograms computed in model P1-4-10% using the amplitude cut-offs.

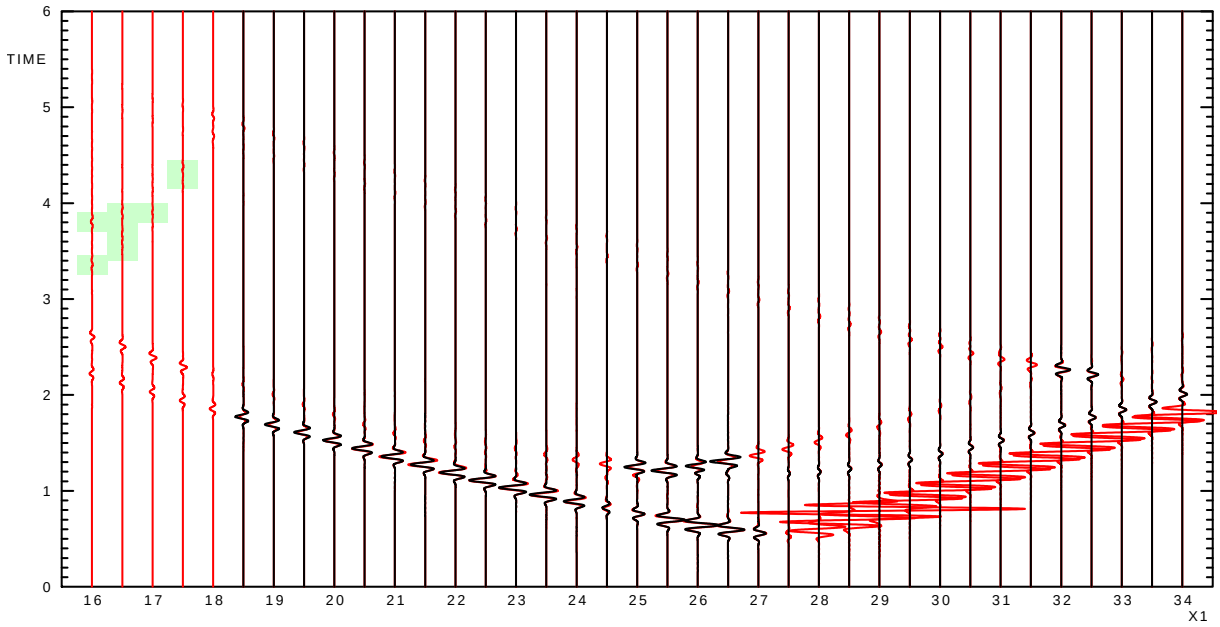

Figure 32: Born (red) and ray-theory (black) seismograms computed in model P1-10-10% using no amplitude cut-off.

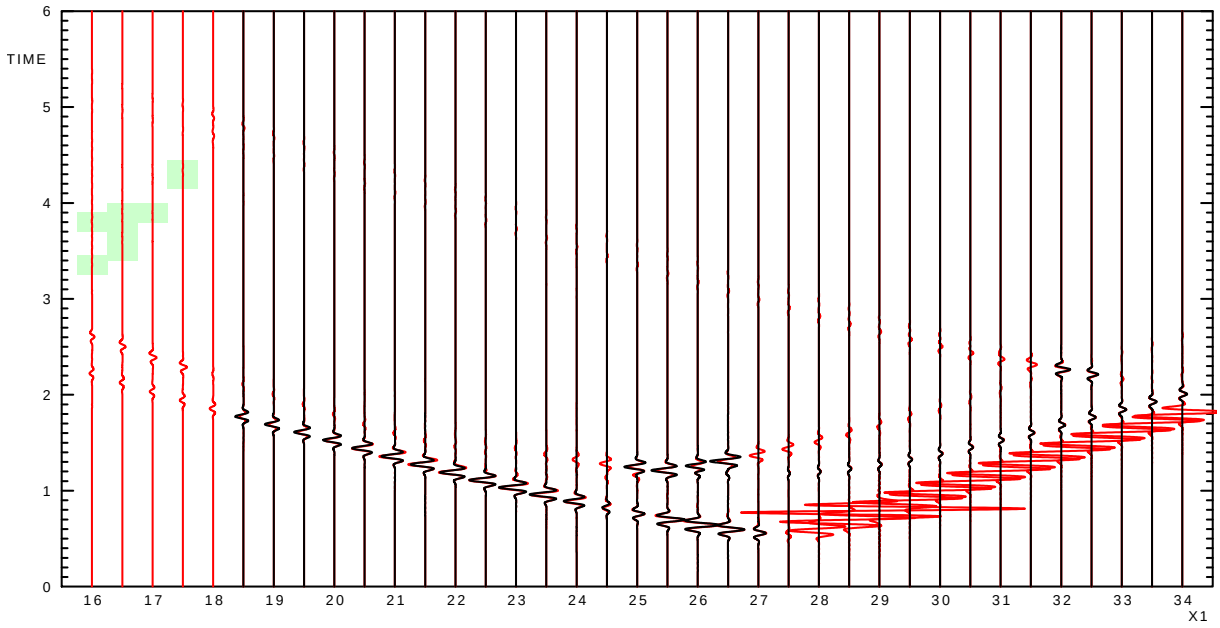

Figure 33: Born (red) and ray-theory (black) seismograms computed in model P1-10-10% using the amplitude cut-offs.

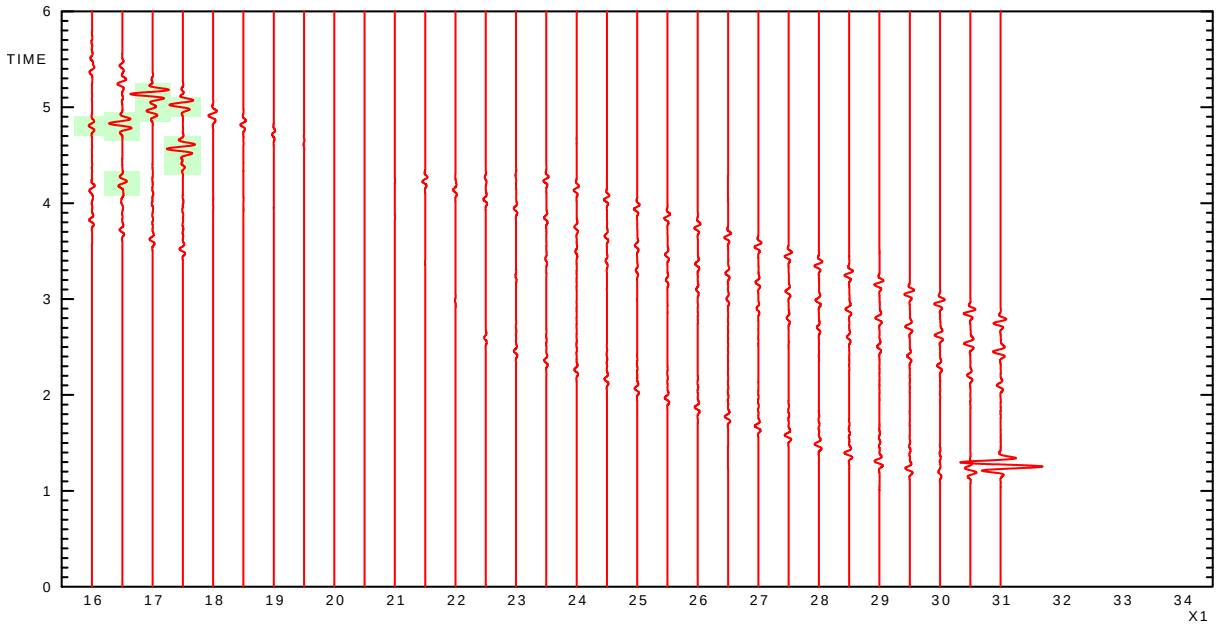

Figure 34: Born (red) and ray-theory (black) seismograms computed in model P1-15-10% using no amplitude cut-off.

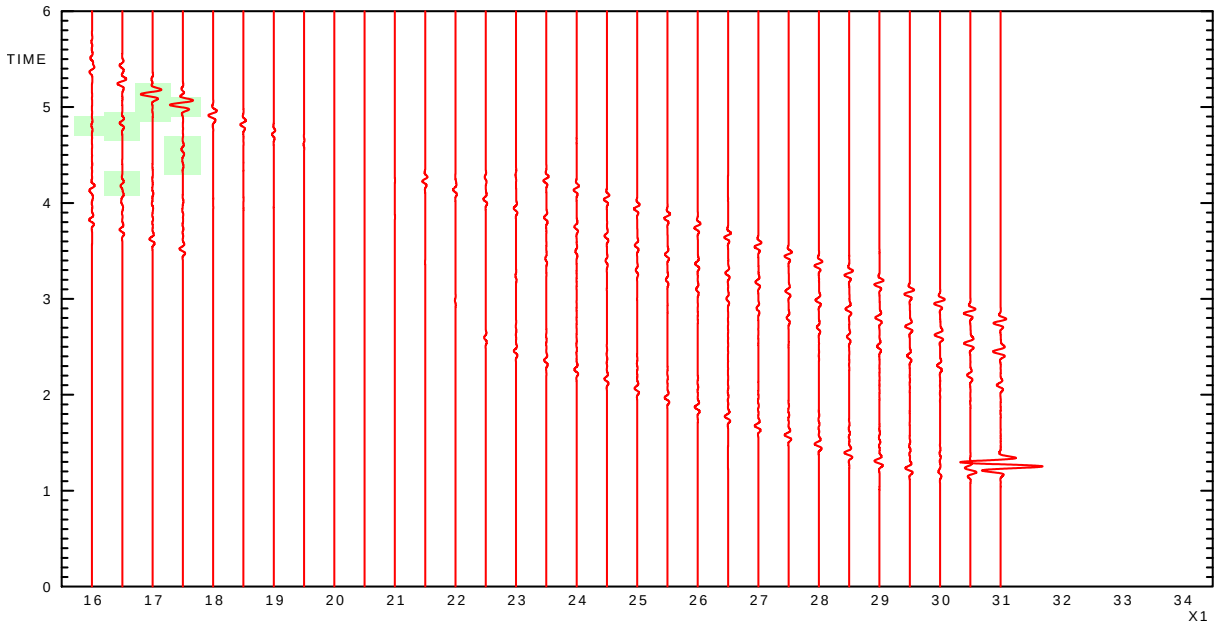

Figure 35: Born (red) and ray-theory (black) seismograms computed in model P1-15-10% using the amplitude cut-offs.

6 Caustics on the reflected wave

So far, we have discussed the problems caused by caustics on the direct wave. However, another effect caused by caustics is still contained in the computed seismograms. The caustics can be present on the reflected wave. The ray-theory seismograms could have significant problems if the receiver is situated at the caustic, or in its close vicinity. The seismogram could be greatly magnified. On the other hand, the Born approximation may not suffer from this problem, because it is computed in the background model where no caustics on the direct wave are present. Moreover, the ray-theory seismograms are zero for the receivers located in the shadow zone. The Born seismograms are non-zero. We observe the diffractions from the caustic.

We present seven examples and comment three of them.

The first example contains the seismograms computed in model P1-5-10%, see Figure 38. We have already seen these seismograms in Figure 21, but now we focus on the strong wavegroup, highlighted in light yellow in the seismograms in Figure 38 for the receiver at $x_1 = 23$ km. The ray diagram of the rays reflected at the interface reached first is depicted in Figure 36. The ray diagram of the rays transmitted through the interface reached first and reflected at the interface reached second is depicted in Figure 37. There are two arrivals for the receivers beween $x_1 = 16$ km and $x_1 = 23$ km in Figure 36. This is the consequence of the caustic. We would probably observe a triplication if the interface did not end suddenly. The ray-theory seismograms depicted in Figure 38 are zero for the receivers between $x_1 = 23.5$ km and $x_1 = 28.5$ km. The Born seismograms smoothly continue to the shadow zone, and the amplitudes of the wavegroups gradually decrease.

The second example contains seismograms computed in model P1-6-10%, see Figure 41. These seismograms have also been already presented, see Figure 23. But now, we are interested in the strong wavegroup, highlighted in light yellow in the seismograms in Figure 41 for the receiver at $x_1 = 28.5$ km. The ray diagrams, which are depicted in Figure 39 and Figure 40, are not very complex. We do not see a triplication for the receiver at $x_1 = 28.5$ km, but it is probably just the consequence of too short an interface. Notice two things. Firstly, the ray-theory seismogram is zero for the receiver at $x_1 = 28$ km, but the Born seismogram is non-zero. Secondly, the Born seismogram is smaller than the ray theory seismogram for the receiver at $x_1 = 28.5$ km, but it matches the ray-theory seismogram for the receiver at $x_1 = 29$ km. It seems that the ray theory has problems due to caustics for the receiver at $x_1 = 28.5$ km, but the Born approximation works well.

In the third example, we present the seismograms computed in model P1-8-10%, see Figure 44. Figures 42 and 43 depict the ray diagrams. In this case, both ray diagrams show triplications of rays. The triplication in Figure 42 is visible between the 18th and 28th receiver, i.e. for the receivers between $x_1 = 24.5$ km and $x_1 = 29.5$ km. The triplication in Figure 43 is visible between the 17th and 23rd receiver, i.e. for the receivers between $x_1 = 24$ km and $x_1 = 27$ km. The first and last receiver, where we observe the triplication in Figure 42 and Figure 43, are highlighted in the seismograms in light blue-green and light yellow, respectively. A continuation of the Born seismograms to the shadow zone is again clearly visible.

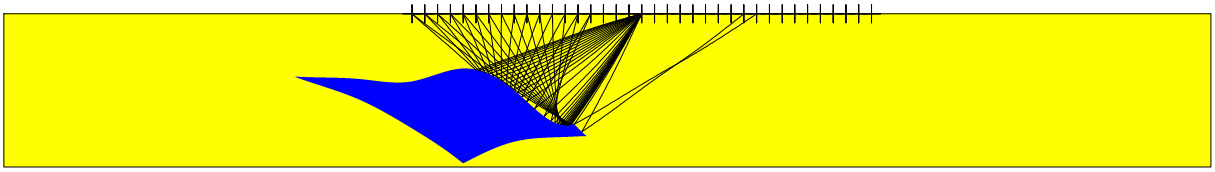

Figure 36: P-wave rays shot from the point source, reflected at the interface reached first and arriving at the profile of receivers in model P1-5-10%.

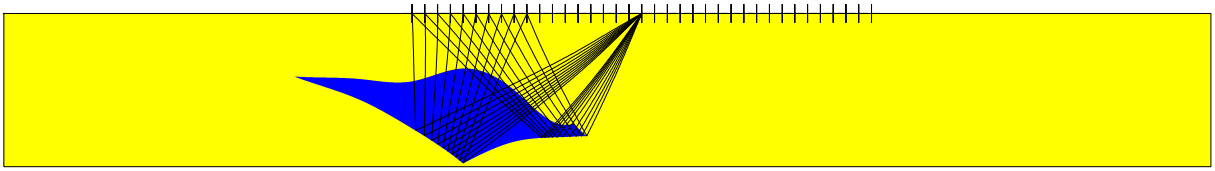

Figure 37: P-wave rays shot from the point source, transmitted through the interface reached first, reflected at the interface reached second and arriving at the profile of receivers in model P1-5-10%.

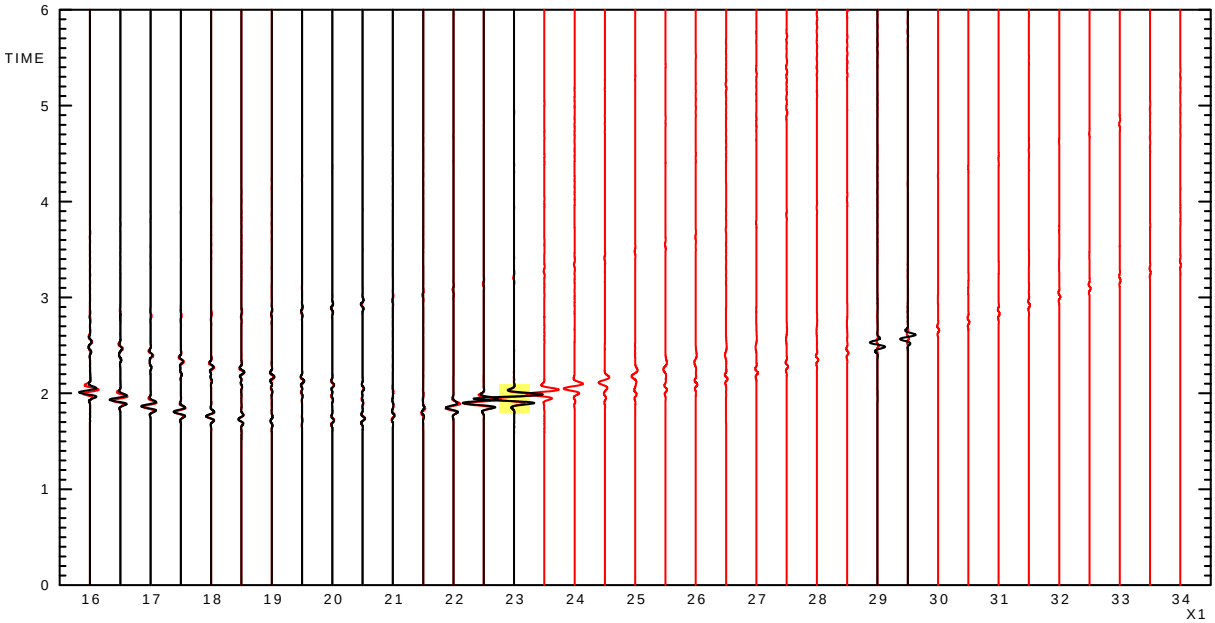

Figure 38: Born (red) and ray-theory (black) seismograms computed in model P1-5-10% using amplitude cut-offs. It seems that the amplitude of the wavegroup in the ray-theory seismograms, highlighted in light yellow, is magnified due to the presence of caustics. The amplitude of the same wavegroup in the Born seismograms should be correct, and we observe a continuation to the shadow zone with the waves diffracted from the caustic.

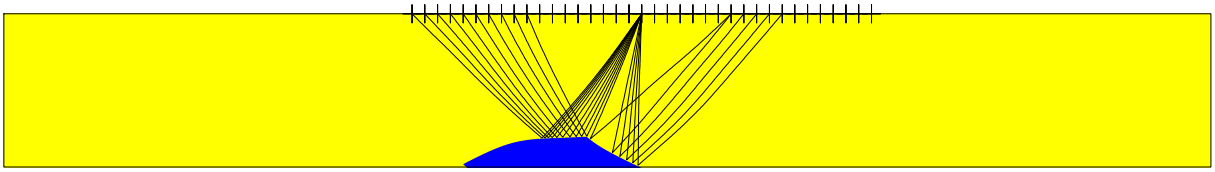

Figure 39: P-wave rays shot from the point source, reflected at the interface reached first and arriving at the profile of receivers in model P1-6-10%.

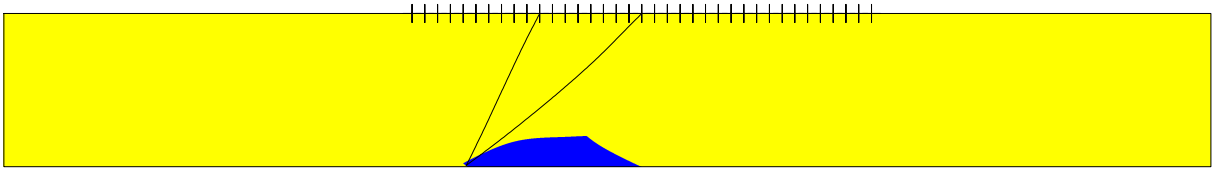

Figure 40: P-wave rays shot from the point source, transmitted through the interface reached first, reflected at the interface reached second and arriving at the profile of receivers in model P1-6-10%.

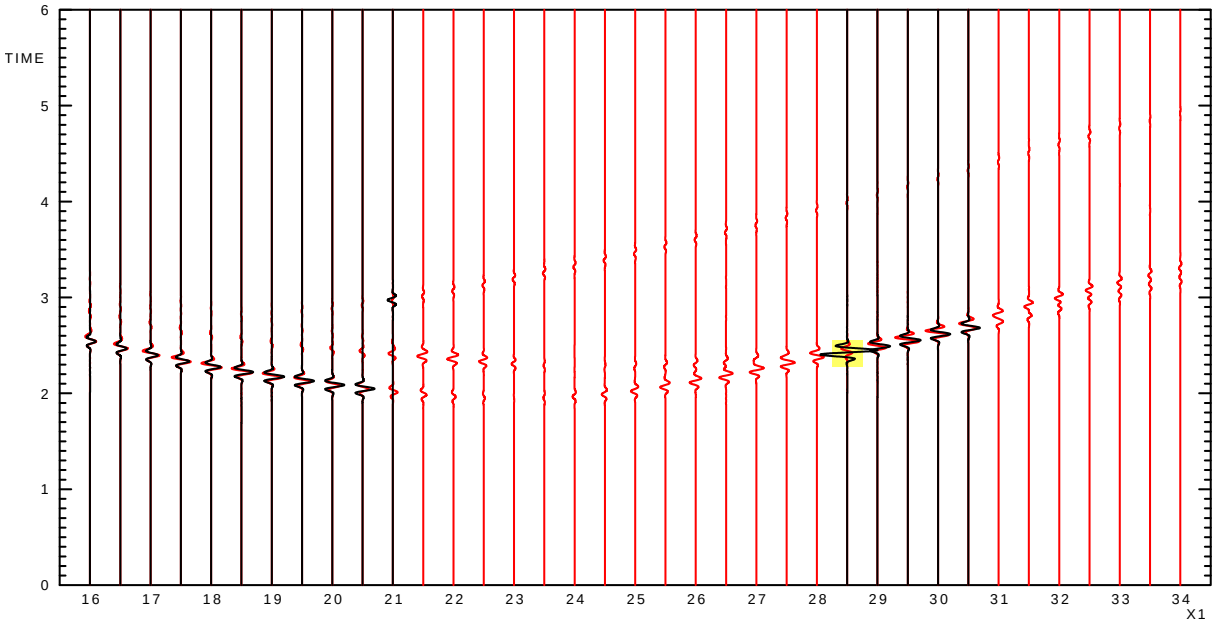

Figure 41: Born (red) and ray-theory (black) seismograms computed in model P1-6-10% using amplitude cut-offs. It seems that the amplitude of the wavegroups in the ray-theory seismograms, highlighted in light yellow, is magnified due to the presence of caustics. The amplitude of the same wavegroup in the Born seismograms should be correct and we observe a continuation to the shadow zone with the waves diffracted from the caustic.

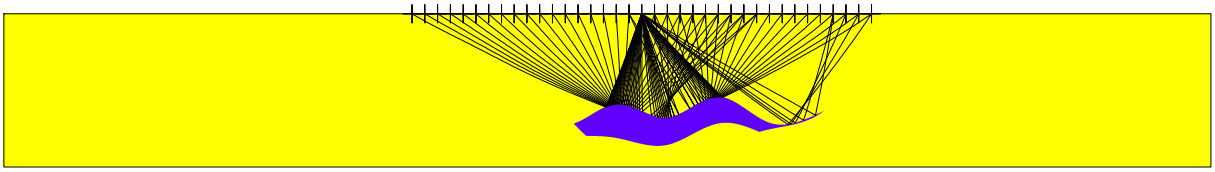

Figure 42: P-wave rays shot from the point source, reflected at the interface reached first and arriving at the profile of receivers in model P1-8-10%.

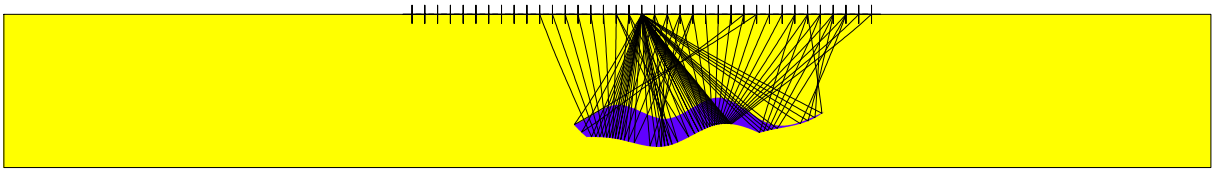

Figure 43: P-wave rays shot from the point source, transmitted through the interface reached first, reflected at the interface reached second and arriving at the profile of receivers in model P1-8-10%.

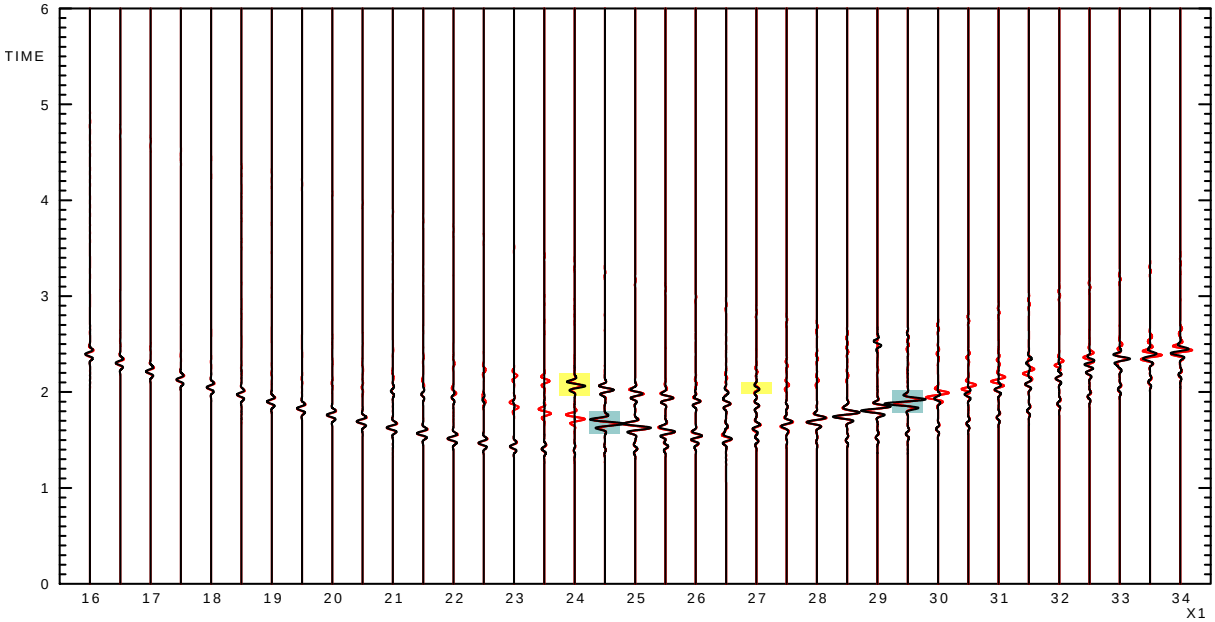

Figure 44: Born (red) and ray-theory (black) seismograms computed in model P1-8-10% using amplitude cut-offs. The wavegroups in the Born seismograms, highlighted in light yellow and light blue-green, continue to the shadow zones with the waves diffracted from the caustics.

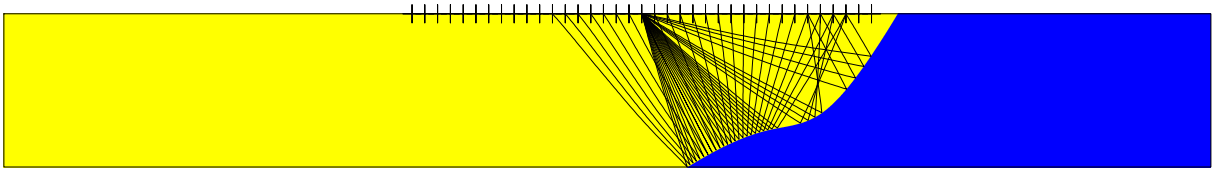

Figure 45: P-wave rays shot from the point source, reflected at the interface reached first and arriving at the profile of receivers in model P1-2-10%.

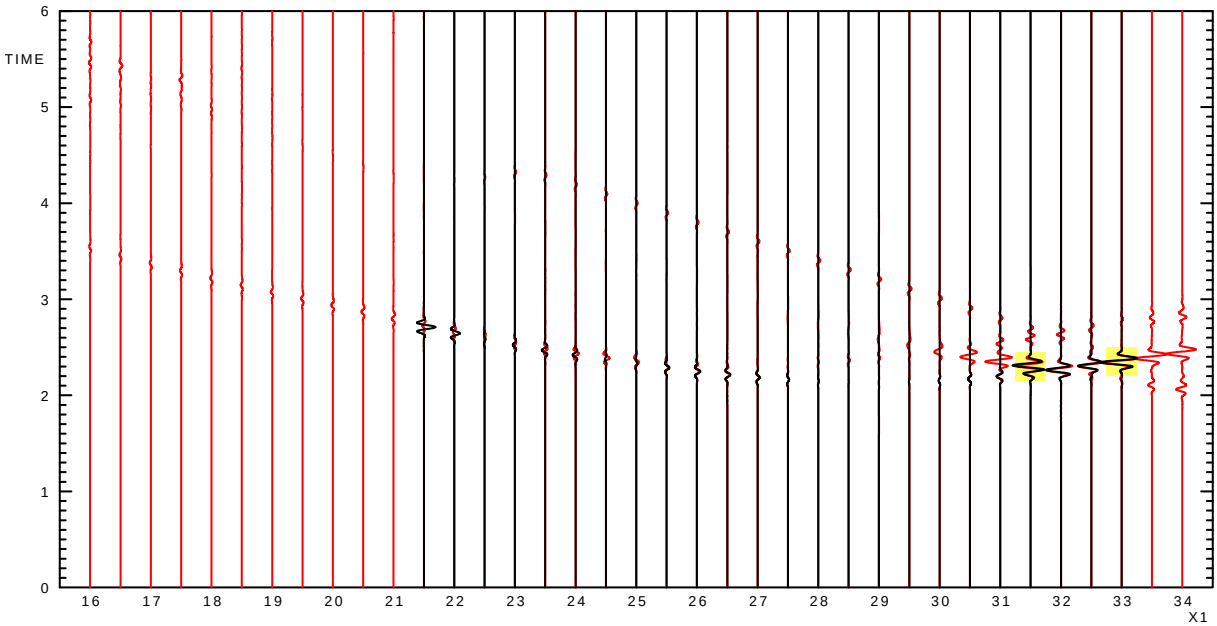

Figure 46: Born (red) and ray-theory (black) seismograms computed in model P1-2-10% using amplitude cut-offs. The wavegroups in the Born seismograms, highlighted in light yellow, continue to the shadow zone with the waves diffracted from the caustic.

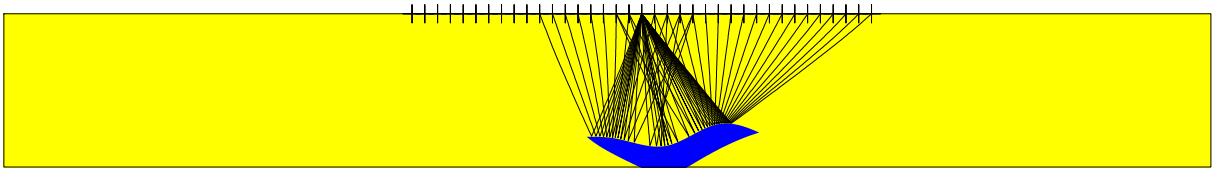

Figure 47: P-wave rays shot from the point source, reflected at the interface reached first and arriving at the profile of receivers in model P1-7-10%.

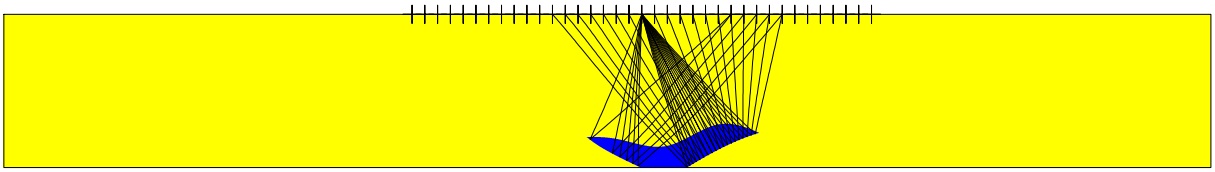

Figure 48: P-wave rays shot from the point source, transmitted through the interface reached first, reflected at the interface reached second and arriving at the profile of receivers in model P1-7-10%.

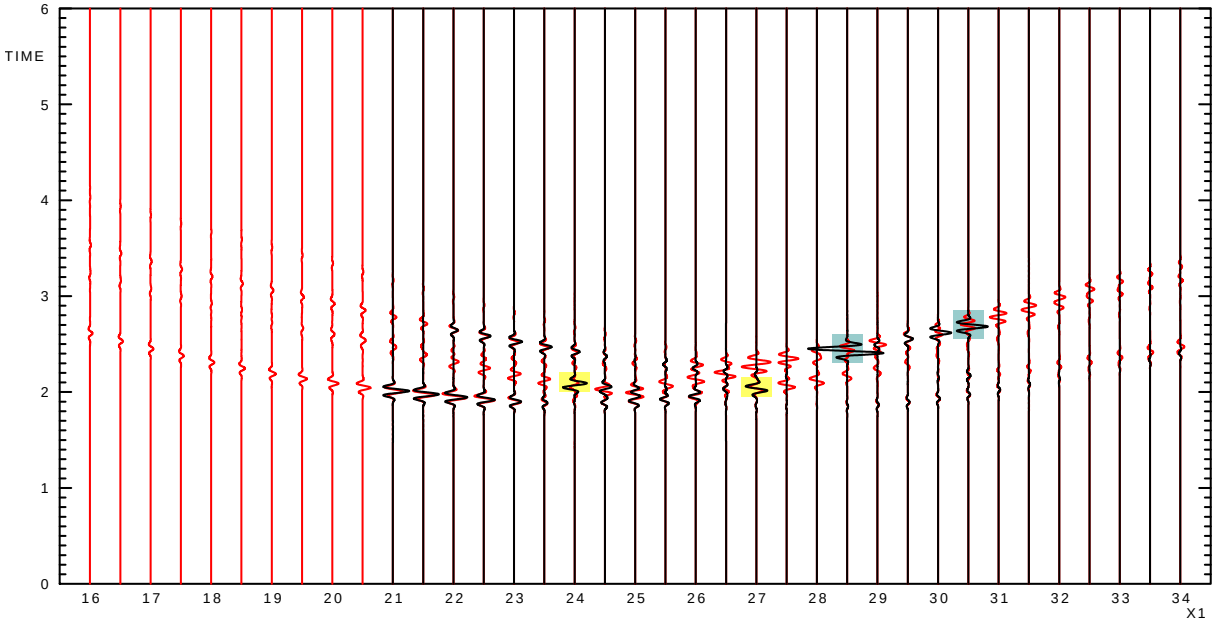

Figure 49: Born (red) and ray-theory (black) seismograms computed in model P1-7-10% using amplitude cut-offs. The wavegroups in the Born seismograms, highlighted in light yellow and light blue-green, continue to the shadow zones with the waves diffracted from the caustics.

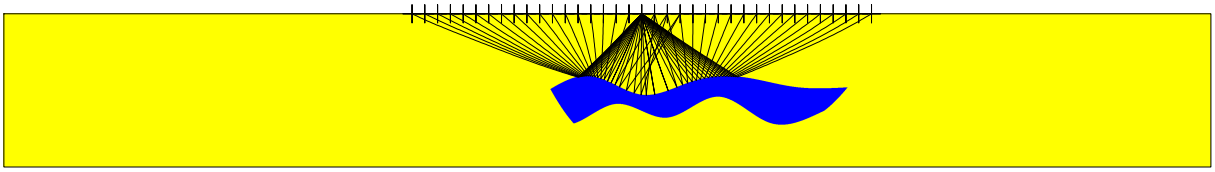

Figure 50: P-wave rays shot from the point source, reflected at the interface reached first and arriving at the profile of receivers in model P1-9-10%.

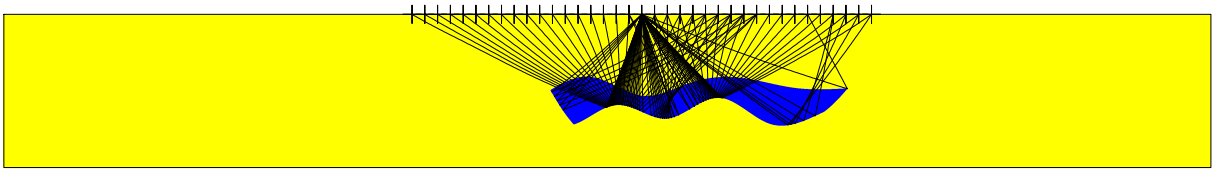

Figure 51: P-wave rays shot from the point source, transmitted through the interface reached first, reflected at the interface reached second and arriving at the profile of receivers in model P1-9-10%.

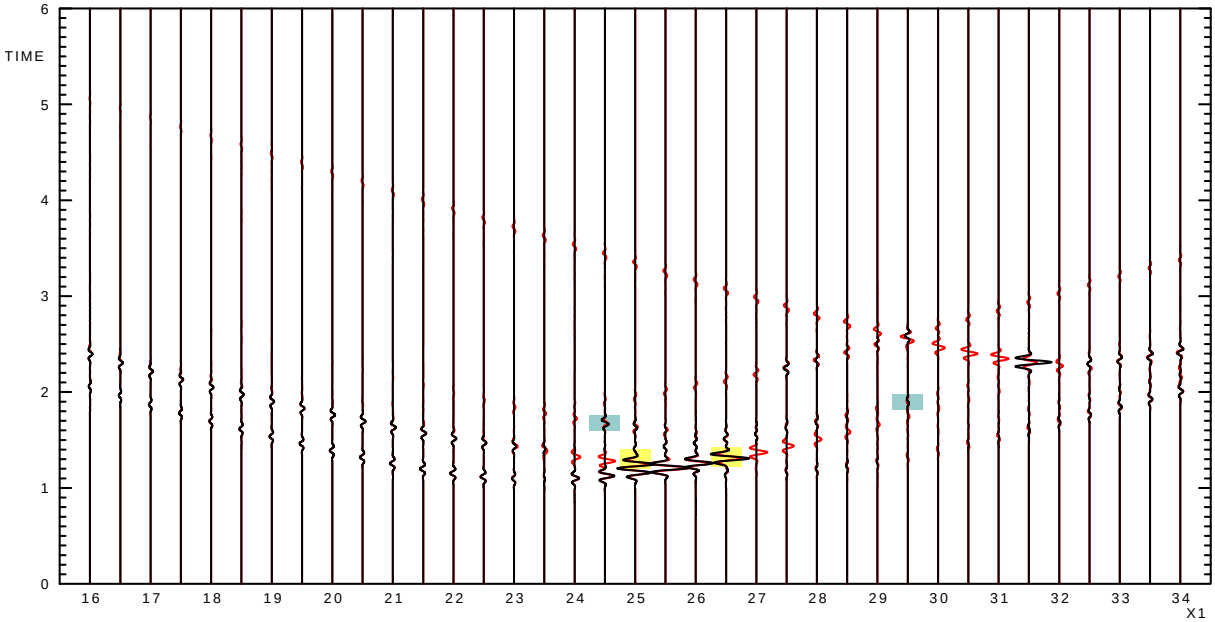

Figure 52: Born (red) and ray-theory (black) seismograms computed in model P1-9-10% using amplitude cut-offs. The wavegroups in the Born seismograms, highlighted in light yellow and light blue-green, continue to the shadow zones with the waves diffracted from the caustics.

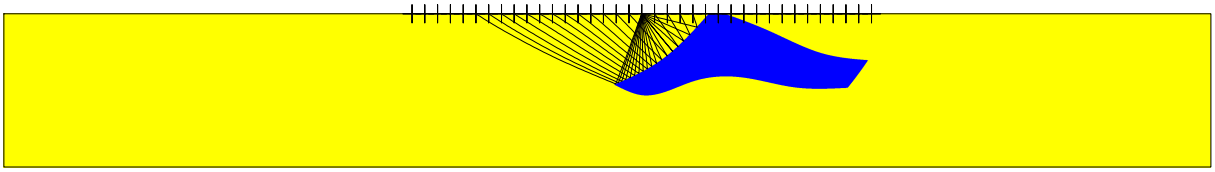

Figure 53: P-wave rays shot from the point source, reflected at the interface reached first and arriving at the profile of receivers in model P1-10-10%.

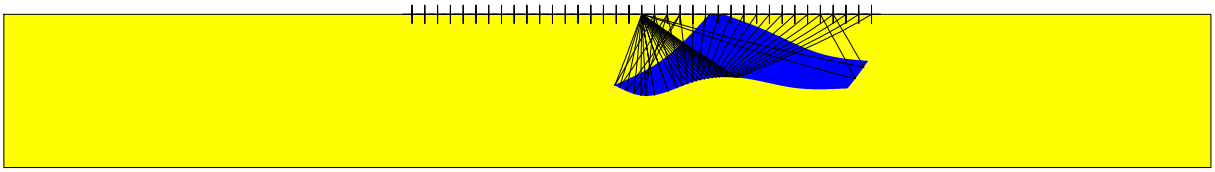

Figure 54: P-wave rays shot from the point source, transmitted through the interface reached first, reflected at the interface reached second and arriving at the profile of receivers in model P1-10-10%.

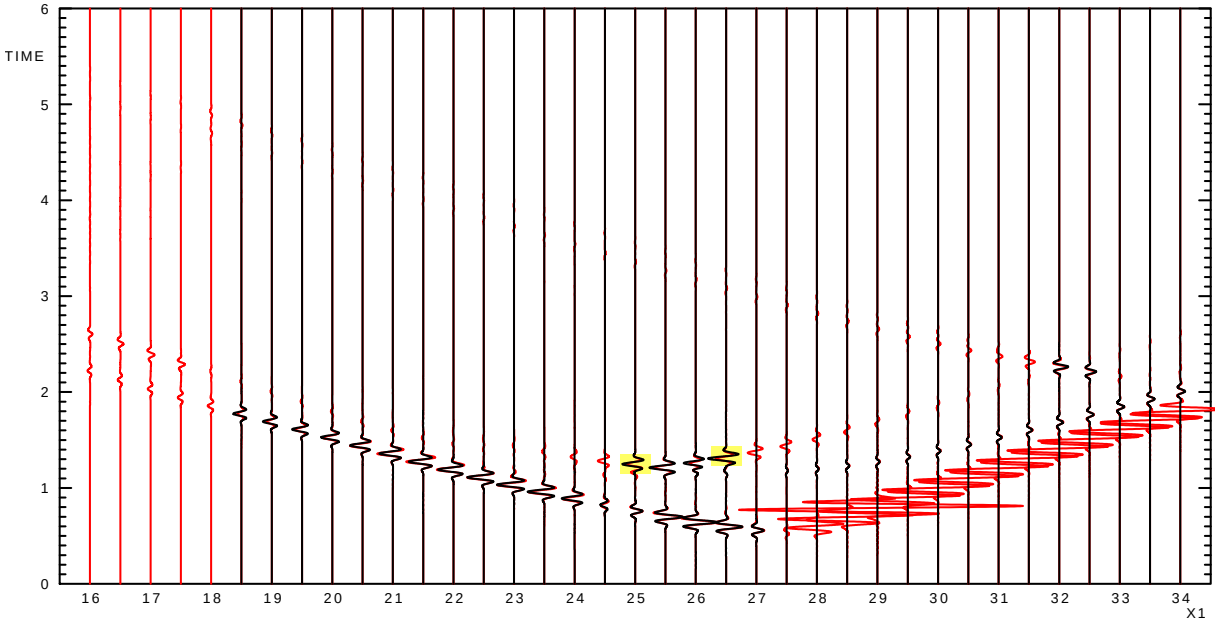

Figure 55: Born (red) and ray-theory (black) seismograms computed in model P1-10-10% using amplitude cut-offs. The wavegroups in the Born seismograms, highlighted in light yellow, continue to the shadow zone with the waves diffracted from the caustic.

7 Concluding remarks

The ray-based Born approximation overcomes some difficulties of the ray theory such as the required smoothness of the model. Unfortunately, also this method has certain problems. One such problem is the generation of strange waves, if caustics are present in the background model. We propose and test a solution of the problem, which consists in cutting the largest amplitudes of the Green function discretized in the computational grid. However, the solution is not fully satisfactory and other possibilities should be sought in the future.

The caustics can also be present on the reflected wave in the perturbed model. The Born approximation is computed in the background model, but the diffractions from the caustics can be observed in the Born seismograms. These diffracted wavegroups are visible also for the receivers in the shadow zone, where the ray-theory seismogram is zero.

Acknowledgements

First of all I would like to thank Luděk Klimeš, who helped me greatly with the work which led to this paper. I would also like to thank Petr Bulant for providing me with model P1 and the history files, which he used for seismogram computation and visualization of the medium parameters. Hence, if I wanted to compute the reference seismogram or to visualize some quantities, I used parts of these history files (or all the history files) and adjusted them as required.

The research has been supported by Grant SVV-2012-265308, by the Grant Agency of the Czech Republic under Contract P210/10/0736, by the Ministry of Education of the Czech Republic within Research Project MSM0021620860, and by the members of the consortium "Seismic Waves in Complex 3-D Structures" (see "http://sw3d.cz").

References

Brokešová, J. (2006): *Asymptotic ray method in seismology: A tutorial.* Matfyzpress, Prague.

Bulant, P. (1999): Two-point ray-tracing and controlled initial-value ray-tracing in 3-D heterogeneous block structures. *J. Seism. Explor.*, **8**, 57-75.

Bulant, P., Martakis, N. (2011): Constructing model P1I for reflection studies. In: *Seismic Waves in Complex 3–D Structures, Report 21*, Dep. Geophys., Charles Univ., Prague, pp. 17-26, online at "http://sw3d.cz".

Červený, V. (2001): *Seismic Ray Theory.* Cambridge University Press, Cambridge.

Červený, V., Coppoli, A. D. M. (1992): Ray-Born synthetic seismograms for complex structures containing scatterers. *J. Seism. Explor.*, **1**, 191-206.

Červený, V., Klimeš, L., Pšenčík, I. (2007): Seismic ray method: Recent developments. *Adv. Geophys.*, **48**, 1-126.

Jin, S., Madariaga, R., Virieux, J., Lambaré, G. (1992): Two-dimensional asymptotic iterative elastic inversion. *Geophys. J. Int.*, **108**, 575-588.

Moser, T. J. (1997): Influence of realistic backgrounds on the validity and performance of ray/Born inversion. *J. Seism. Explor.*, **6**, 239-252.

Moser, T. J. (2012): Review of ray-Born forward modeling for migration and diffraction analysis. *Stud. Geophys. Geod.*, **56**, No.2.

Šachl, L. (2011): 2D computations of 3D synthetic seismograms using the ray-based Born approximation in heterogeneous background model P1. In: *Seismic Waves in Complex 3–D Structures, Report 21*, Dep. Geophys., Charles Univ., Prague, pp. 99-114, online at "http://sw3d.cz".

Šachl, L. (2012): Born and ray-theory seismograms in 2D heterogeneous isotropic models. *Seismic Waves in Complex 3–D Structures, Report 22*, Dep. Geophys., Charles Univ., Prague, pp. 83-112.

Thierry, P., Operto, S., Lambaré, G. (1999): Fast 2-D ray+Born migration/inversion in complex media. *Geophysics*, **64**, No. 1, 162-181.

Vavryčuk, V. (2003): Parabolic lines and caustics in homogeneous weakly anisotropic solids. *Geophys. J. Int.*, **152**, 318-334